DETECTION OF UNIVERSALITY OF DARK MATTER PROFILE FROM SUBARU WEAK LENSING MEASUREMENTS
OF 50 MASSIVE CLUSTERS

Hiroko Niikura [1,2], Masahiro Takada[1], Nobuhiro Okabe[1,3], Rossella Martino[4], Ryuichi Takahashi[5]
[1] Kavli Institute for the Physics and Mathematics of the Universe (Kavli IPMU, WPI), UTIAS, The University of Tokyo, Chiba, 277-8583, Japan
[2] Physics Department, The University of Tokyo, Bunkyo, Tokyo 113-0031, Japan
[3]Department of Physical Science, Hiroshima University, 1-3-1 Kagamiyama, Higashi-Hiroshima, Hiroshima 739-8526, Japan
[4] Laboratoire AIM, IRFU/Service d'Astrophysique-CEA-CNRS, Bt. 709, CEA-Saclay, 91191 Gif-sur-Yvette Cedex, France
[5]Faculty of Science and Technology, Hirosaki University, 3 Bunkyo-cho, Hirosaki, Aomori 036-8561, Japan
To be submitted to PASJ

ABSTRACT

We develop a novel method of measuring the lensing distortion profiles of clusters with stacking the "scaled" amplitudes of background galaxy ellipticities as a function of the "scaled" centric radius according to the Navarro-Frenk-White (NFW) prediction of each cluster, based on the assumption that the different clusters in a sample follow the *universal* NFW profile. First we demonstrate the feasibility of this method using both the analytical NFW model and simulated halos in a suite of high-resolution *N*-body simulations. We then apply, as a proof of concept, this method to the Subaru weak lensing data and the *XMM/Chandra* X-ray observables for a sample of 50 massive clusters in the redshift range $0.15 \leq z \leq 0.3$, where their halo masses differ from each other by up to a factor of 10. To estimate the NFW parameters of each cluster, we use the halo mass proxy relation of X-ray observables, based on either the hydrostatic equilibrium or the gas mass, and then infer the halo concentration from the model scaling relation of halo concentration with halo mass. We evaluate a performance of the NFW scaling analysis by measuring the scatters of 50 cluster lensing profiles relative to the NFW predictions over a range of radii, $0.14 \leq R/[h^{-1}\mathrm{Mpc}] \leq 2.8$. We found a $4 - 6\sigma$ level evidence of the universal NFW profile in 50 clusters, for both the X-ray halo mass proxy relations, although the gas mass appears to be a better proxy of the underlying true mass. By comparing the measurements with the simulations of cluster lensing profiles taking into account the statistical errors of intrinsic galaxy shapes in the Subaru data, we argue that additional halo mass errors or intrinsic scatters of $\sigma(M_{500c})/M_{500c} \sim 0.2 - 0.3$ could reconcile a difference between the measurements and the simulations. This method allows us to some extent to preserve characteristics of individual clusters in the statistical weak lensing analysis, thereby yielding a new means of exploiting the underlying genuine form of the halo mass profile and the halo mass proxy relations via weak lensing information, under the assumption of the existence of the universal profile.

Subject headings: cosmology: observations – dark matter – galaxies: clusters: general – gravitational lensing: weak

1. INTRODUCTION

Clusters of galaxies are the largest, gravitationally bound objects in the Universe, and the formation and evolution processes are dominated by gravitational effects mainly due to dark matter. Hence clusters provide us with a useful laboratory for studying the nature of dark matter (Clowe et al. 2006) as well as constraining cosmology, e.g. from the abundance of clusters found from a survey volume (Vikhlinin et al. 2009; Rozo et al. 2010; Oguri & Takada 2011). However, to attain the full potential of cluster-based cosmology from upcoming wide-area surveys such as the Subaru Hyper Suprime-Cam[1] and the Dark Energy Survey[2] requires a further understanding of the physical processes in clusters.

One of the most important predictions in *N*-body simulations of the Λ-dominated, cold dark matter structure formation model (ΛCDM) is the emergence of universal mass density profile – that is, the mass density profile of dark matter halos can be well fitted by a "universal" two-parameter family of the model profile over a wide range of halo masses, first proposed in Navarro et al. (1996, 1997, hereafter NFW). The NFW profile predicts a monotonically steepened profile with increasing radius, with logarithmic slopes shallower than

an isothermal sphere interior to the characteristic "scale" radius $r < r_s$, but steeper at larger radius, approaching r^{-3} at the virial radius, $r \rightarrow r_{\mathrm{vir}}$ (see also Dalal et al. 2010, for discussion on the physical origin within the framework of the hierarchical ΛCDM model). Further, the ratio of the characteristic scale radius to the virial radius, which characterizes the degrees of central concentration of the mass distribution – the so-called halo concentration c – tends to be lower for more massive halos. In addition the halo concentration of a fixed halo mass displays intrinsic scatters typically given by $\sigma_{\ln c} \sim 0.2$, originating from details of the mass accretion or assembly history of each halo in the hierarchical structure formation (Bullock et al. 2001; Wechsler et al. 2002; Zhao et al. 2003; Duffy et al. 2008; Zhao et al. 2009; Bhattacharya et al. 2013; Diemer & Kravtsov 2015). Thus these properties of dark matter halos are important predictions of ΛCDM model, and need to be carefully tested by measurements.

Gravitational lensing is a unique, powerful method enabling one to probe the matter distribution in galaxy clusters irrespective of their physical and dynamical states (Schneider 2006). Several works have investigated the mass density profile over a wide range of radii by combining the strong and weak lensing at the small and large radii, observationally the exquisite high-resolution images of Hubble Space Telescope and the wide-field ground based telescopes such as the Subaru

[1] http://www.naoj.org/Projects/HSC/j_index.html
[2] http://www.darkenergysurvey.org

Telescope (Tyson & Fischer 1995; Kneib et al. 2003; Broadhurst et al. 2005; Smith et al. 2005; Oguri et al. 2005, 2012; Hoekstra et al. 2012; Newman et al. 2013; Zitrin et al. 2014; Merten et al. 2014). In addition, the stacked weak lensing analysis combining a sample of clusters has been proven to be a robust, powerful method of probing the average mass distribution of the sampled clusters (Johnston et al. 2007; Okabe et al. 2010a; Oguri et al. 2012; Okabe et al. 2013; Umetsu et al. 2014). These works have shown that the average mass profile measured from the stacked lensing is in remarkably nice agreement with the NFW prediction. Another advantage of stacked lensing is it allows one to probe the mass distribution even for less massive halos, such as galaxy-scale halos, as long as a sufficient number of sampled halos (e.g. galaxies) are used in the analysis (Mandelbaum et al. 2005; Leauthaud et al. 2010; Miyatake et al. 2013). However, a downside of the stacked lensing method is the loss of lensing information of individual clusters. Hence a knowledge of the distribution of the underlying halo parameters in the sampled clusters such as their halo masses is of critical importance in order not to have any bias in the NFW parameters inferred from the stacked lensing signals (Oguri & Takada 2011). This is equivalent to the importance of exploring a well-calibrated proxy relation of cluster observables with halo mass or more generally halo parameters (Rozo et al. 2009; Zhang et al. 2010; Okabe et al. 2010b; Zhang et al. 2011; Mahdavi et al. 2013; von der Linden et al. 2014; Martino et al. 2014; Okabe et al. 2014; Hoekstra et al. 2015).

The purpose of this paper is to develop a novel method of measuring the lensing distortion profiles of clusters, motivated by the NFW prediction. We propose the "NFW scaling" analysis for the lensing measurements, which is done by averaging the "scaled" amplitudes of background galaxy ellipticities in each bin of the "scaled" radii according to the NFW prediction of individual cluster. With this NFW scaling method, we can address whether clusters display the universality of their lensing profiles as seen in simulations. First, to demonstrate the feasibility of the NFW scaling analysis, we will use simulations of cluster lensing observables based on a suite of high-resolution N-body simulations. Then, as a proof of concept, we will apply this method to a sample of 50 massive clusters in the redshift range $0.15 \leq z \leq 0.3$ that have been observed with the Subaru telescope by the Local Cluster Substructure Survey (LoCuSS, and also see Okabe et al. 2010a, 2013; Martino et al. 2014, for details)[3]. Note that this study is based on the published results of LoCuSS, and is not performed within the collaboration. To estimate the NFW scaling of each cluster, we will use the halo mass estimate in Martino et al. (2014) based on the *XMM* and/or *Chandra* X-ray observables, and use the halo concentration inferred from the model scaling relation between halo mass and concentration in Diemer & Kravtsov (2015). Then by comparing the scatters of 50 cluster lensing profiles relative to the NFW predictions for two cases with and without the NFW scaling, we test the performance of this method as well as the universality of the cluster mass distribution.

The structure of this paper is as follows. In § 2, after briefly reviewing the lensing observables of NFW halo, we will derive an estimator of the lensing distortion profile measurement with NFW scaling. Then we study the feasibility of this

method using analytical NFW models and N-body simulations. In § 3, we first describe the Subaru weak lensing catalog and the X-ray observables for the sample of massive clusters we use in this paper, and show the results of the application of this method to the Subaru data. § 4 is devoted to discussion and conclusion. Unless stated otherwise, we will adopt a flat ΛCDM cosmology with $\Omega_m = 0.27$, $\Omega_\Lambda = 0.73$, and the Hubble parameter $h = H_0/(100 \text{ km s}^{-1}\text{Mpc}^{-1}) = 0.70$.

2. METHODOLOGY: STACKED WEAK LENSING WITH NFW SCALING

2.1. *Lensing of Navarro-White-Frenk halo*

The Navarro-Frenk-White (1997; hereafter NFW) mass density profile for a halo is parametrized by two parameters as

$$\rho_{\text{NFW}}(r) = \frac{\rho_c}{(r/r_s)(1 + r/r_s)^2}, \qquad (1)$$

where r_s is the scale radius and ρ_c is the central density parameter. The parameter ρ_c is specified by imposing that the mass enclosed within a sphere of a given overdensity Δ is equal to the halo mass M_Δ,

$$\rho_c = \frac{\Delta \rho_{\text{cr}}(z) c_\Delta^3}{3 m_{\text{NFW}}(c_\Delta)} = \frac{M_\Delta}{4\pi r_s^3 m_{\text{NFW}}(c_\Delta)}, \qquad (2)$$

where $m_{\text{NFW}}(c_\Delta) \equiv \int_0^{c_\Delta} dx \, x/(1+x)^2 = \ln(1+c_\Delta) - c_\Delta/(1+c_\Delta)$, $c_\Delta \equiv r_\Delta/r_s$, a concentration parameter, and $\Delta(z)$ is a nonlinear overdensity introduced to define the interior mass for each halo. Note that throughout this paper we employ halo mass definition with respect to the critical density, not the mean mass density: $M_\Delta \equiv (4\pi/3)r_\Delta^3 \rho_{\text{cr}}(z)\Delta$. Although we focus on the NFW profile in this paper, the method developed in this paper can be applied to any other univeral profile such as generalized NFW or Einasto profile (Einasto 1965; Merritt et al. 2006).

Several works have shown a scaling relation of the halo concentration with halo mass, using numerical simulations or based on analytical arguments (Bullock et al. 2001; Wechsler et al. 2002; Zhao et al. 2003; Duffy et al. 2008) (most recently Diemer & Kravtsov 2015, hereafter DK15 and see references therein). As for our fiducial model, we adopt the publicly-available code provided by B. Diemer to compute the halo mass and concentration relation in DK15. Note that we used the "median" relation, rather than the mean, for our default choice as recommended in DK15. The mass estimates from the X-ray observables are not M_{200c}, and rather the interior mass of a greater overdensity such as M_{500c}. Assuming that a halo exactly follows the NFW profile, we can convert the scaling relation calibrated for M_{200c} to the c_{500c}-M_{500c} relation, based on the method in Hu & Kravtsov (2003). The public code of DK15 allows us to compute the halo concentration for an input overdensity based on this method. We will also study how possible variations in the c-M relation affect the results of this paper.

For an NFW profile, we can derive an analytical expression for the lensing convergence and shear profiles (Bartelmann 1996; Golse & Kneib 2002):

$$\kappa^{\text{NFW}}(R) \equiv \frac{\Sigma^{\text{NFW}}(R)}{\Sigma_{\text{cr}}(z_l, z_s)} = 2\rho_c r_s \frac{g^{\text{NFW}}(R/r_s)}{\Sigma_{\text{crit}}(z_l, z_s)},$$

$$\gamma_+^{\text{NFW}}(R) \equiv \frac{\Delta\Sigma^{\text{NFW}}(R)}{\Sigma_{\text{cr}}(z_l, z_s)} = 2\rho_c r_s \frac{f^{\text{NFW}}(R/r_s)}{\Sigma_{\text{crit}}(z_l, z_s)}, \qquad (3)$$

---

where R is the projected comoving radius from halo center, and the functions $f^{\mathrm{NFW}}(x)$ and $g^{\mathrm{NFW}}(x)$ are given by

$$
g^{\mathrm{NFW}}(x) = \begin{cases} \dfrac{1}{x^2-1}\left(1 - \dfrac{1}{\sqrt{1-x^2}}\cosh^{-1}\dfrac{1}{x}\right), & (x < 1) \\[2ex] \dfrac{1}{3}, & (x = 1) \\[2ex] \dfrac{1}{x^2-1}\left(1 - \dfrac{1}{\sqrt{x^2-1}}\cos^{-1}\dfrac{1}{x}\right), & (x > 1) \end{cases} \quad (4)
$$

and

$$
f^{\mathrm{NFW}}(x)
$$
$$
= \begin{cases} \dfrac{2}{x^2}\ln\dfrac{x}{2} + \dfrac{1}{1-x^2}\left(1 + \dfrac{2-3x^2}{x^2\sqrt{1-x^2}}\cosh^{-1}\dfrac{1}{x}\right), & (x < 1) \\[2ex] \dfrac{5}{3} - 2\ln 2, & (x = 1) \,(5) \\[2ex] \dfrac{2}{x^2}\ln\dfrac{x}{2} - \dfrac{1}{x^2-1}\left(1 + \dfrac{2-3x^2}{x^2\sqrt{x^2-1}}\cos^{-1}\dfrac{1}{x}\right), & (x > 1). \end{cases}
$$

The critical surface mass density Σ_{crit} for a given system of lens cluster and source at redshifts z_l and z_s, respectively, is given as

$$
\Sigma_{\mathrm{crit}}(z_l, z_s) = \frac{c^2}{4\pi G}\frac{D_A(z_s)}{D_A(z_l)D_A(z_l, z_s)(1+z_l)^2}, \quad (6)
$$

where $D_A(z)$ is the angular diameter distance and the factor $(1+z_l)^2$ is from our use of the comoving scale. From Eqs. (2) and (3), we can find that the lensing amplitudes of an NFW halo scale with the NFW parameters (M_Δ, c_Δ) as

$$
\kappa^{\mathrm{NFW}}, \gamma_+^{\mathrm{NFW}} \propto 2\rho_c r_s \propto M_\Delta \Big/\left(r_s^2 m_{\mathrm{NFW}}(c_\Delta)\right)
$$
$$
\propto M_\Delta^{1/3} c_\Delta^2 / m_{\mathrm{NFW}}(c_\Delta). \quad (7)
$$

If we employ the c_Δ-M_Δ scaling relation given as $c_\Delta(M_\Delta) \propto M^{-\alpha}$, the lensing amplitudes roughly scale with halo mass as $\gamma_+^{\mathrm{NFW}} \propto M^{1/3-2\alpha}$ as the function $m(c_\Delta)$ has a weak dependence on halo mass. Note that, since the cluster sample is among the most massive clusters, we have checked that the 2-halo term is much smaller than the above 1-halo term, by a factor of 100, over a range of the radii we consider (e.g., see Oguri & Takada 2011; Takada & Spergel 2014). Therefore we ignore the 2-halo term for the following analysis.

An actual lensing observable estimated from ellipticities of background galaxies for an NFW lens is the lensing "distortion" profile or reduced shear profile:

$$
\langle e_+ \rangle (R) \rightarrow \frac{\gamma_+^{\mathrm{NFW}}(R)}{1 - \kappa^{\mathrm{NFW}}(R)}, \quad (8)
$$

where e_+ is the tangential component of the ellipticities with respect to cluster center. The reduced shear correction is not negligible at the inner radii, and we need to take into account the correction.

2.2. Stacked lensing without NFW scaling

For the standard method to estimate the stacked lensing profile for N_c clusters, we follow the method in Johnston et al. (2007) and Mandelbaum et al. (2013):

$$
\widehat{\langle\Delta\Sigma\rangle}(R) = \frac{1}{N}\sum_{a=1}^{N_c}\sum_{s_a;|\mathbf{R}_{(a)s_a}|\in R} w_{(a,s_a)}\Sigma_{\mathrm{cr}(a)} e_{(s_a)+}(\mathbf{R}_{s_a}), \quad (9)
$$

where $e_{(s_a)+}$ is the tangential ellipticity of the s_a-th background galaxy in the a-th cluster region, and N is the normalization factor defined as

$$
N = \sum_{a=1}^{N_c}\sum_{s_a} w_{(a,s_a)}. \quad (10)
$$

The summation $\sum_a$ runs over the sampled clusters, from $a = 1$ to N_c, and the summation $\sum_{s_a;|\mathbf{R}_{s_a}|\in R}$ runs over all the background galaxies that reside in the annulus of radius R from the a-th cluster center to within the bin width. We employ the weight given as

$$
w_{(a,s_a)} = \frac{1}{\Sigma_{\mathrm{cr}}(z_a, z_{s_a})^2 (e_{(s_a)}^2 + \sigma_{(s_a)e}^2 + \alpha^2)}, \quad (11)
$$

where z_{s_a} is the redshift of the s_a-th background galaxy, $e_{(s_a)}$ is the ellipticity amplitude, $\sigma_{(s_a)e}$ is the measurement error and α is the constant factor to regularize the weight for which we adopt $\alpha = 0.4$ (Okabe et al. 2010a). Note that we employ the average redshift for all the source galaxies in each cluster region, as described below in detail.

Since we need to employ a finite number of the radial bins to study the "shape" of lensing distortion profile, which binning scheme to use is not so clear. As for the representative value of a given radial bin, we use the average of radii of background galaxies that reside in the annulus taking into account their weights:

$$
R \equiv \frac{\sum_{a=1}^{N_c}\sum_{s_a;|\mathbf{R}_{(a)s_a}|\in R} w_{(a,s_a)} R_{(a)s_a}}{\sum_{a=1}^{N_c}\sum_{s_a;|\mathbf{R}_{(a)s_a}|\in R} w_{(a,s_a)}}. \quad (12)
$$

In the literature the area-weighted value of each radial bin is often used. We have checked that, using an analytical NFW profile and taking the actual distribution of background galaxies in the Subaru data, the above radial binning is more accurate in the sense that the distortion profile is in better agreement with the model NFW profile amplitude inferred by the representative value of the radial bin, less than 1% in the fractional difference for most cases.

The statistical uncertainty of the stacked lensing at each radial bin can be estimated as

$$
\sigma_{\langle\Delta\Sigma\rangle}(R)^2 = \frac{1}{2N^2}\sum_{a=1}^{N_c}\sum_{s_a;|\mathbf{R}_{(a)s_a}|\in R} w_{(a,s_a)}^2 \Sigma_{\mathrm{cr}(a)}(z_a, z_{s_a})^2 e_{(s_a)}^2. \quad (13)
$$

In this paper we consider the intrinsic ellipticities as a source of the statistical errors in the lensing measurement, and ignore the cosmic shear contribution that arises from different mass distribution along the same line of sight to the cluster. For the application of this method to the Subaru data that we will show below, this is a good approximation in practice, because the mean number density of background galaxies is small, about 5 arcmin^{-2}, after a secure selection of background "red" galaxies as we will discuss in § 3.1.1 (also see Okabe et al. 2013, for the details).

When comparing the measured lensing profile to an NFW model, we need to account for the contribution of reduce shear. In this paper, assuming that all the clusters follow a single NFW profile in average sense, we model the the stacked

lensing profile, according to Eqs. (3) and (8) as

$$
\begin{aligned}
\langle\widehat{\Delta\Sigma}\rangle(R) &\Longleftrightarrow \frac{\Delta\Sigma^{\mathrm{NFW}}(R)}{1-\kappa^{\mathrm{NFW}}(R)} \\
&\simeq \Delta\Sigma^{\mathrm{NFW}}(R)\left[1+\left\langle\frac{1}{\Sigma_{\mathrm{cr}}}\right\rangle\Sigma^{\mathrm{NFW}}(\langle R\rangle)\right], \quad (14)
\end{aligned}
$$

where the notation " $\Longleftrightarrow$ " is meant to denote the comparison between the measurement (left-hand side) and the model profile (right-hand side). The notation $\langle\ \ \rangle$ on the right-hand side denotes the average taking into account the weights of background galaxies in each cluster region as in Eq. (12). We will use the above equation to estimate the halo mass and concentration parameter, M_{Δ} and c_{Δ}, from the measured lensing profile.

2.3. *Stacked lensing with NFW scaling*

Now we consider the stacked lensing analysis with "NFW scaling". To implement this method we combine the weak lensing measurement and X-ray observables, where the X-ray observables are needed to estimate halo mass of each cluster independently of the lensing observables. Assuming that each of the sampled clusters follows an NFW profile specified by their respective parameters, $M_{(a)}$ and $c_{(a)}$, we can define an estimator of the *normalized* NFW lensing profile from the measured ellipticities of background galaxies, as motivated by Eq. (3):

$$
\langle\widehat{f^{\mathrm{NFW}}}\rangle(x) = \frac{1}{N}\sum_{a=1}^{N_c}\sum_{s_a;|\mathbf{x}_{(a)s_a}|\in x}\frac{w_{(a,s_a)}\Sigma_{\mathrm{cr}(a)}e_{(s_a)+}(\mathbf{x}_{s_a})}{2\rho_c\left(M_{(a)}^{\mathrm{X}},c_{(a)}^{\mathrm{X}}\right)r_s\left(M_{(a)}^{\mathrm{X}},c_{(a)}^{\mathrm{X}}\right)}.
$$
(15)

Here $M_{(a)}^{\mathrm{X}}$ and $c_{(a)}^{\mathrm{X}}$ are the halo mass and concentration for the a-th cluster, estimated from the X-ray observables (see below for details). The *scaled* radius in the above equation, x, is defined for the a-cluster as $\mathbf{x}_{(a)s_a} \equiv \mathbf{R}_{(a)s_a}/r_s(M_{(a)}^{\mathrm{X}},c_{(a)}^{\mathrm{X}})$, where r_s is the scale radius of NFW profile, $r_s = r_{\Delta}/c_{\Delta}$. We use the representative value of each radial bin, x, defined in a similar manner to Eq. (12). The central density parameter of NFW profile, ρ_c, can be estimated from $M_{(a)}^{\mathrm{X}}$ and $c_{(a)}^{\mathrm{X}}$ for the a-th cluster, from Eq. (2). Note that the profile $\langle\widehat{f^{\mathrm{NFW}}}\rangle$ and the radius x are dimension-less. With the above NFW scaling, weak lensing signals due to less massive halos than the mean mass in the sampled clusters are up-weighted, while the signals of more massive halos are down-weighted.

Similarly, the measurement errors of the stacked profile at each radial bin are estimated as

$$
\sigma_{\langle f^{\mathrm{NFW}}\rangle}(x)^2 = \frac{1}{2N^2}\sum_{a=1}^{N_c}\sum_{s_a;|\mathbf{x}_{(a)s_a}|\in x}\frac{w_{(a,s_a)}^2\Sigma_{\mathrm{cr}(a)}(z_a,z_{s_a})^2e_{(s_a)}^2}{4\rho_c\left(M_{(a)}^{\mathrm{X}},c_{(a)}^{\mathrm{X}}\right)^2r_s\left(M_{(a)}^{\mathrm{X}},c_{(a)}^{\mathrm{X}}\right)^2}.
$$
(16)

To test an improvement in the stacked lensing analysis of NFW scaling compared to the standard stacked lensing, we compare the scatters of lensing distortion profiles of the sampled clusters relative to the NFW prediction. To be more precise, we quantify the scatters by

$$
d^2 \equiv \sum_{a=1}^{N_c}\sum_i\frac{\left[\widehat{\Delta\Sigma_{(a)}}(R_{(a)i})-\Delta\Sigma^{\mathrm{bf-NFW}}(R_{(a)i};M_{\mathrm{bf}},c_{\mathrm{bf}})\right]^2}{\sigma_{\Delta\Sigma(a)}(R_{(a)i})^2}
$$
(17)

or

$$
d_{\mathrm{w-scaling}}^2 \equiv \sum_{a=1}^{N_c}\sum_i\frac{\left[\widehat{f_{(a)}^{\mathrm{NFW}}}(x_{(a)i})-f^{\mathrm{NFW}}(x_{(a)i})\right]^2}{\sigma_{f^{\mathrm{NFW}}(a)}(x_{(a)i})^2}.
$$
(18)

Here $\widehat{\Delta\Sigma_{(a)}}$ and $\widehat{f_{(a)}^{\mathrm{NFW}}}$ are the measured distortion profile without and with NFW scaling for the a-th cluster, which are estimated in the similar manner to Eqs. (9) and (15), and $\sigma_{\Delta\Sigma(a)}$ and $\sigma_{f^{\mathrm{NFW}}(a)}$ are the errors at each radial bin, estimated similarly to Eqs. (13) and (16), respectively. $\Delta\Sigma^{\mathrm{bf-NFW}}(R)$ is the best-fit NFW profile of the stacked lensing profile (Eq. 14). For the NFW scaling case, we similarly include the reduced shear correction: we multiply the function $f^{\mathrm{NFW}}(x)$ (Eq. 5) by the function, $1 + \langle 1/\Sigma_{\mathrm{cr}}\rangle_{w_{(a,s_a)}}\Sigma^{\mathrm{NFW}}(x)$ as in Eq. (14), where we used the best-fit NFW model of the stacked lensing profile without NFW scaling in order to compute $\Sigma^{\mathrm{NFW}}(x)$. The above d^2 and $d_{\mathrm{w-scaling}}^2$ are equivalent to the log-likelihood functions of lensing distortion profiles of N_c clusters assuming that the statistical errors are given by the intrinsic ellipticities. The radial bin $R_{(a)i}$ or $x_{(a)i}$ for the a-th cluster is similarly computed by Eq. (12) from the background galaxies that reside in the annulus of the cluster. However, comparing the scatters of lensing distortion profiles with and without NFW scaling requires a careful treatment of the radial binning. As we will later describe in more detail, we will employ the radial binning scheme so as to preserve the same background galaxies in the i-th radial bins with or without the NFW scaling. With this binning scheme, the relation $d^2 = d_{\mathrm{w-scaling}}^2$ holds if setting the model profiles to $\Delta\Sigma^{\mathrm{bf-NFW}} = f^{\mathrm{NFW}} = 0$ [4]. If the lensing distortion profiles of the sampled clusters are similar in their shapes and amplitudes, following the NFW profile, the value of d^2 should become smaller: $d_{\mathrm{w-scaling}}^2 < d^2$.

2.4. *Testing the method with N-body simulations*

In this subsection, before going to the Subaru data, we test our method using analytical NFW model and high-resolution N-body simulations. For the sake of convenience to compare with the following sections, we consider 50 clusters in this section as the 50 Subaru clusters.

First let's consider an ideal case, albeit unrealistic, that each of 50 clusters *exactly* follows an NFW profile. Figure 1 shows the lensing profiles with or without the NFW scaling for 50 halos. To take into account variations in halo masses that resemble the 50 clusters, we assign one-by-one the X-ray inferred masses of 50 cluster to NFW halos [5]. Note that we use the c-M scaling relation in DK15 to compute the halo concentration for each NFW halo. The different blue curves show each NFW distortion profile relative to the best-fit NFW model of the stacked distortion profile, as a function of the radius relative to the scale radius of the best-fit NFW model. Here we consider the same range of radii, $0.14 \le R/[h^{-1}\mathrm{Mpc}] \le 2.8$ for all the halos as we will do for actual analysis of Subaru data. For the range of cluster masses, the lensing distortion amplitudes differ from each other by up to a factor of 5.

---

[4] If we set $\Delta\Sigma^{\mathrm{bf-NFW}} = f^{\mathrm{NFW}} = 0$ in Eqs. (17) and (18), the values of d^2 give the cumulative signal-to-noise ratio of the lensing distortion measurements for the N_c clusters.

[5] We here employed the hydrostatic equilibrium mass in Martino et al. (2014), which was estimated from the X-ray observables of each cluster.
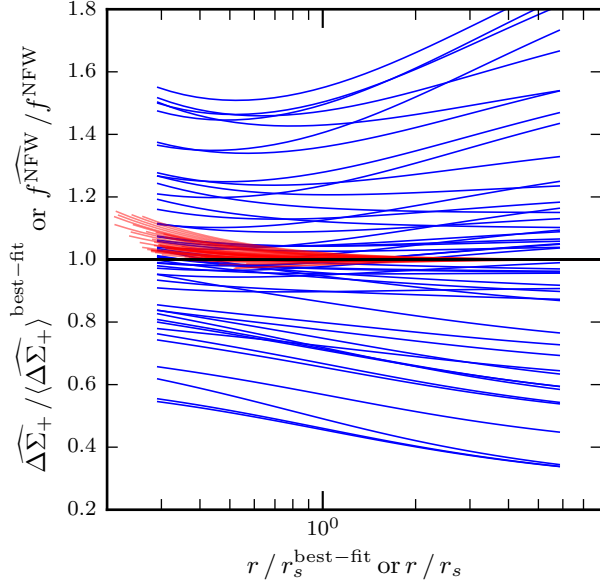
Figure 1. The distribution of NFW lensing profiles for 50 halos for each of which we took the X-ray inferred mass of 50 Subaru clusters (here the hydrostatic equilibrium mass in Table 1) and assumed the halo concentration based on the halo mass and concentration relation, $c = c(M_{500c})$, in Diemer & Kravtsov (2015, hereafter DK15). The blue curves are the lensing profiles without "NFW scaling", i.e. the standard method, but each curve is normalized by the best-fit NFW profile to the stacked profile of 50 profiles, and is plotted as a function of the radius relative to the scale radius of the best-fit NFW model. The red curves are the lensing profiles with "NFW scaling", computed assuming that the halo mass and concentration of each halo are *a priori* known – an ideal case. Note that we fixed the same range of radii, $0.14 < R/[h^{-1}\mathrm{Mpc}] < 2.8$, in the comoving length units for both the results.

On the other hand, the red curves in Figure 1 show the profiles after the NFW scaling implementation, assuming that the true mass and concentration of each cluster are *a priori* known, i.e. an ideal case. Each curve is the fractional profile relative to the NFW distortion profile including the reduced shear correction, $f^{\mathrm{NFW}}(x)$ (Eq. 5 and see below Eq. 15). The deviation from unity is due to an imperfect correction of the reduced shear: the nonlinear correction becomes non-negligible at small radii, and breaks the universality of the NFW lensing profile. The horizontal axis is in the units of the "scaled" radius, R/r_s, where r_s is the NFW scale radius of each halo. Due to the radial transformation from the original fixed range of R, the range of the scaled radius x, covered by each halo, differ from each other. The figure shows that the NFW scaling significantly reduces the scatters of lensing profiles, making the differences within 20% over a range of radii we consider.

Obviously actual clusters have much more complicated mass distribution than an analytical NFW model: intrinsic scatters of halo concentration, aspherical mass distribution, substructures and so on. To study these effects we use simulated halos of cluster scales, generated from a high-resolution N-body simulation in Takahashi et al. (2012). In brief the N-body simulation was ran with the publicly-available *Gadget-2 code* (Springel et al. 2001; Springel 2005) assuming the WMAP cosmology. The simulation employed 1024^3 particles in a box of $320\ h^{-1}\mathrm{Mpc}$ on a side. The mass resolution (the particle mass) is $2.3 \times 10^9\ h^{-1}M_\odot$, so is sufficient to resolve cluster-scale halos.

To construct a catalog of cluster-scale halos from the N-

body simulation output at $z = 0$, we used the friends-of-friends (FoF) group finder (e.g. Davis et al. 1985) with a linking length of 0.2 in units of the mean interparticle spacing. For each halo we determined the halo center using an iterative technique in which the center of mass of particles within a shrinking sphere is computed recursively until a few particles are left inside (e.g. Power et al. 2003; Masaki et al. 2013). Then the halo mass is defined by a spherical overdensity method – summing all the particles within a sphere of a given overdensity Δ around the halo center. We constructed a catalog that consists of most massive 50 halos from the two simulation realizations. Besides the mass threshold, we did not employ any other selection criteria such as sphericity or the degree of mass distribution complexity. The mean mass of the selected halos is similar to the average mass estimated from the lensing measurements of 50 Subaru clusters (see Figure 2). Exactly speaking, although the simulated halos are not the *same* in detail as the Subaru clusters, other effects such as the intrinsic ellipticities of background galaxies cause much larger variations in the lensing profiles as we will show later. Hence we believe that the catalog of simulated halos is suitable enough for our purpose.

To test our method as well as to simulate the lensing observables from the above N-body simulations, we use the following procedures:

- *3D mass density profile* – We first computed the spherically-average mass profile for each simulated halo, $\rho(r)$, where r is the three-dimensional radius from the halo center. Then we estimated the NFW parameters, M_Δ and c_Δ for $\Delta = 500$, by fitting the model NFW profile (Eq. 1) to the mass profile, where we weighted the simulated mass density profile at a given radial bin by the volume of the spherical shell. We stored the best-fit parameters $(M_{500c}^{\mathrm{3D\ fit}}, c_{500c}^{\mathrm{3D\ fit}})$ for each of the 50 halos.

- *2D lensing profiles* – To simulate the lensing profiles due to a simulated halo, we use the dark matter (N-body) particles inside or surrounding the halo in the simulation output. We estimated the shear profile of each halo by projecting the N-body particles along the line-of-sight direction:

$$\Delta\Sigma(R) = \langle\Sigma\rangle(<R) - \bar{\Sigma}(R). \quad (19)$$

Here we chose the z-direction of simulation realization for the projection, and R is the projected radius from the halo center in the xy-plane (the plane perpendicular to the projection direction). $\langle\Sigma\rangle(<R)$ is the averaged surface mass density within a circle of radius R, and $\bar{\Sigma}(R)$ is the averaged surface mass density over the annulus of radius R. In this projection calculation, we used a cubic region containing the halo at the center, whose side length is $20\ h^{-1}\mathrm{Mpc}$. Since the shear field arises from the tidal field around a halo, the constant mass density field or the mass density field beyond the cubic region causes a negligible contribution to distortion of background galaxies. We checked that the cubic box is large enough for the range of radii we consider. We included the reduced shear correction to compute the distortion profile of the halo, which is a direct lensing observable:

$$\widehat{\Delta\Sigma}(R) = \frac{\Delta\Sigma(R)}{1 - \Sigma(R)/\Sigma_{\mathrm{cr}}(z_\mathrm{l}, z_\mathrm{s})}, \quad (20)$$

where $\Sigma_{\mathrm{cr}}(z_\mathrm{l}, z_\mathrm{s})$ is the lensing efficiency. In doing so
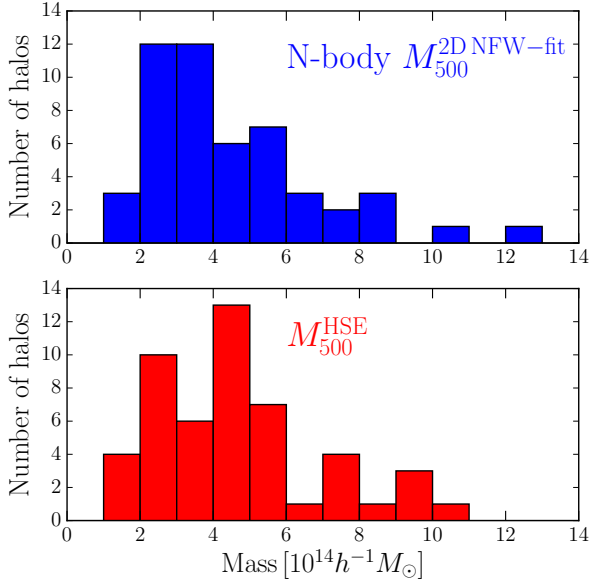
Figure 2. The distribution of halo masses in 50 clusters, taken from the *N*-body simulations (see text for details) or estimated based on the X-ray observables (here we used the hydrostatic equilibrium method).
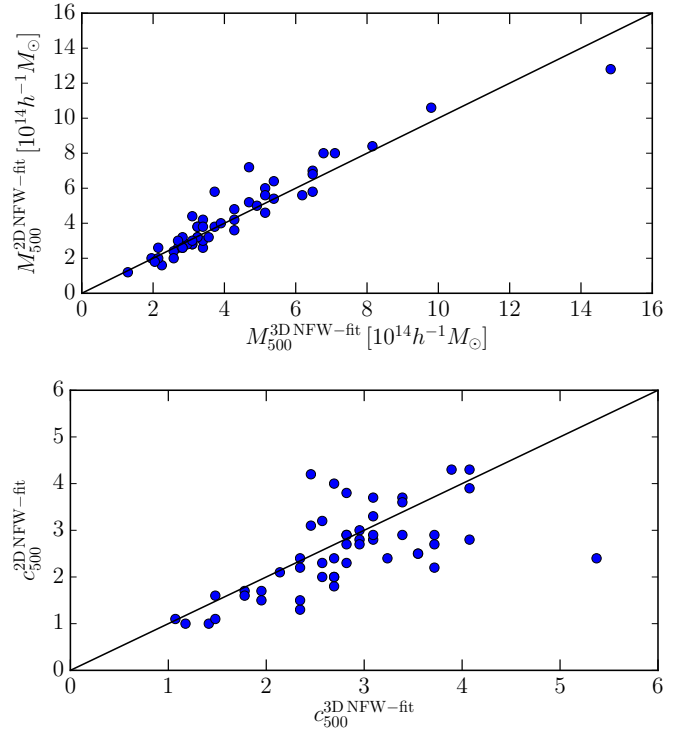

Figure 3. Comparison of the best-fit NFW parameters, halo mass and concentration, estimated by fitting the NFW model to the three-dimensional mass density profile ("3D NFW-fit") or the two-dimensional lensing distortion profile ("2D NFW-fit"), respectively, for the 50 massive halos in *N*-body simulations of ΛCDM model, respectively (see § 2.4 for details). The mean halo mass and the range of their halo masses of simulated halos are similar to those of 50 Subaru clusters.

we assign the source and cluster redshifts of each of the 50 Subaru clusters to each simulated halo one-by-one in descending order of halo masses, where we used the hydrostatic equilibrium mass of X-ray observables in this matching. The assignment of Σ_{cr} becomes relevant when we will include the effect of background shape noise in the Subaru data on the simulated lensing signals of *N*-body halos. We estimated the NFW profile parameters, $(M_{500c}^{2D}, c_{500c}^{2D})$, by fitting the NFW lensing profile (Eq. 14) to the above simulated profile. In this fitting we weighted the lensing profile at each radial bin by the area of radial annulus. We stored the distortion profile, the lensing efficiency function, $\Sigma_{cr}(z_l, z_s)$, and the best-fit NFW parameters $(M_{500c}^{2D\,fit}, c_{500c}^{2D\,fit})$ for each of the 50 simulated halos.

In Figure 2 we compare the distribution of halo masses of simulated halos (upper panel) and 50 clusters (lower), where we used the best-fit NFW mass for the simulated 2D lensing profile for each simulated halo and used the X-ray hydrostatic equilibrium mass for each cluster. The figure shows that the simulated halos cover the similar range of halo masses as in the Subaru clusters.

Figure 3 compares the best-fit NFW parameters, M_{500c} and c_{500c}, estimated by fitting the NFW model to the three-dimensional mass density profile or the two-dimensional lensing distortion profile for each of the 50 simulated halos. Even if we did not include any effect of measurement errors, the NFW parameters inferred from the 3D or 2D fitting generally differ on individual halo basis. For some halos the 2D fitting halo mass is larger than the 3D fitting mass, while the 2D concentration is smaller than the 3D one. These over- or under-estimation would be due to the *c-M* degeneracy in the NFW fitting. These biases might cause a source of systematic errors in estimating the NFW parameters from the lensing observables and then testing the ΛCDM simulation predictions, e.g. whether or not the *c-M* scaling relation inferred from the lensing observables is consistent with the *N*-body simulation predictions (e.g. Okabe et al. 2010a, 2013; Umetsu et al.

2014). This is not the main purpose of this paper, but would be worth to further study.

In Figure 4 we performed a hypothetical experiment of the stacked lensing analyses with and without NFW scaling, using the 50 simulated halos. Note that we here ignored shape noise contribution for simplicity. First, the upper-left panel shows the stacked lensing profile as well as the lensing profiles of individual halos, without NFW scaling, i.e. based on the standard method. Again note that we used a fixed range of radial bins, $0.14 \leq R/[h^{-1}\mathrm{Mpc}] \leq 2.8$ as we will do for the real data. The scatters of individual lensing profiles are significant over a range of the radii. Each profile shows various features due to the aspherical mass distribution, in contrast to an analytical, spherical NFW profile. Interestingly, however, the figure shows that the average profile after stacking appears to remarkably well match the NFW profile; the stacked profile and the best-fit NFW profile are almost indistinguishable, on top of each other. For the sake of comparison we plot the amplitudes and the radius relative to the best-fit NFW model of the stacked profile as in Figure 1: the best-fit parameters are $M_{500c}^{bf} \simeq 4 \times 10^{14}\ h^{-1} M_\odot$ and $c_{500c}^{bf} \simeq 2.50$. These numbers are compared to the averages of their underlying true values: $\langle M_{500c}^{3D\,fit} \rangle \simeq 4.38 \times 10^{14} h^{-1} M_\odot$, $\langle c_{500c}^{3D\,fit} \rangle \simeq 2.76$ or $\langle M_{500c}^{2D\,fit} \rangle \simeq 4.56 \times 10^{14} h^{-1} M_\odot$ and $\langle c_{500c}^{2D\,fit} \rangle \simeq 2.57$. Thus the stacked lensing tends to underestimate the true mass, confirming the claims in the previous work (Mandelbaum et al. 2005; Meneghetti et al. 2010; Becker & Kravtsov 2011; van den Bosch et al. 2013; Meneghetti et al. 2014).

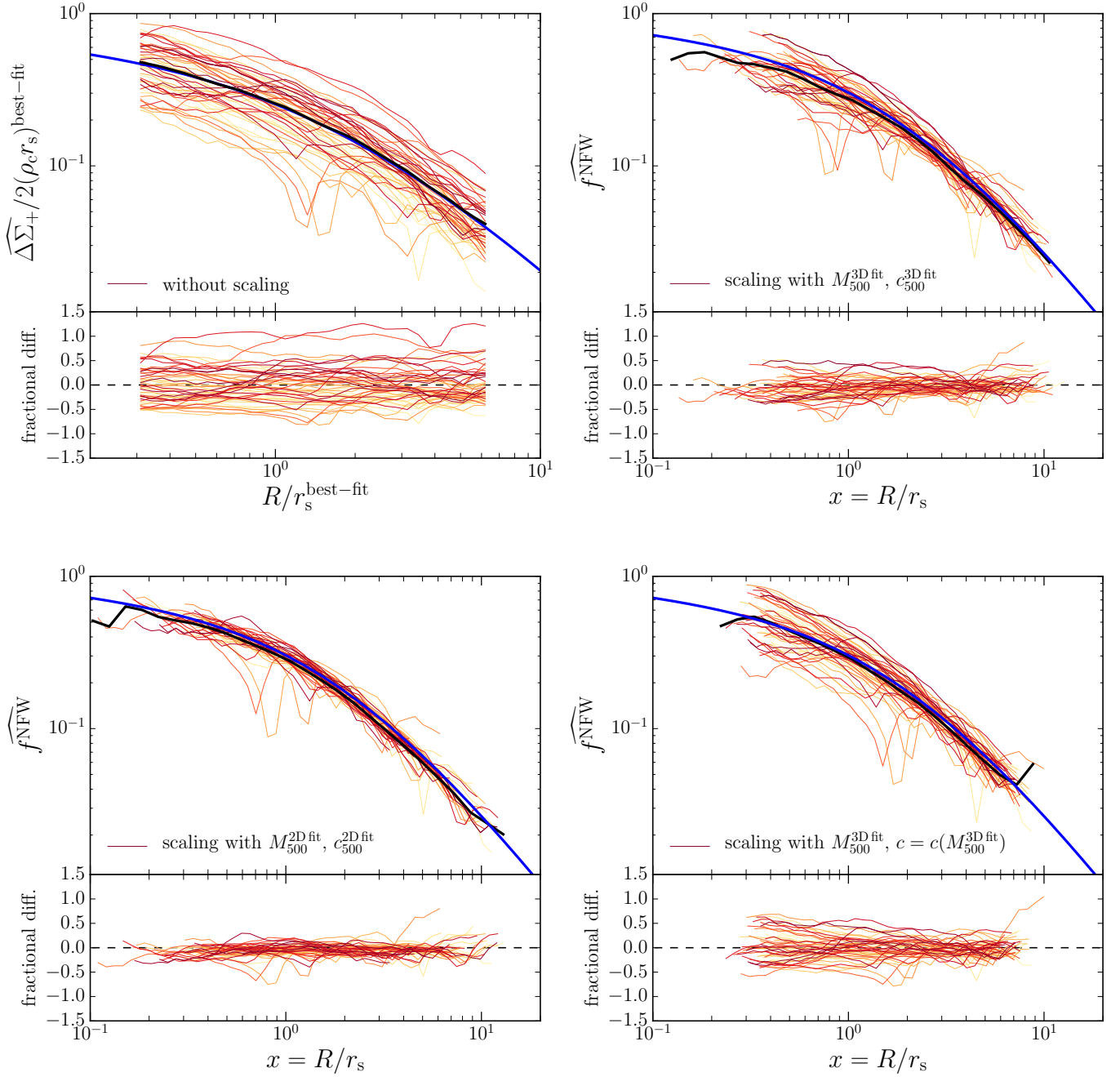The other three panels show the results with NFW scal-

Figure 4. Simulated lensing profiles for 50 massive halos in the *N*-body simulation (see § 2.4 for details). *Upper-left panel*: The thin curves show the lensing profiles for each of the 50 halos, and the bold black curve is the stacked lensing profile without NFW scaling. The blue curve is the best-fit NFW profile to the stacked profile. As in Figure 1, we plot these profiles in terms of the "scaled" amplitude, $\widehat{\Delta\Sigma_+}/(2\rho_c r_s)^{\mathrm{bf-NFW}}$, as a function of the "scaled" projected radius, $R/r_s^{\mathrm{bf-NFW}}$, where we used the best-fit NFW parameters of the stacked profile (blue curve). Hence both the quantities in the *x*- and *y*-axes are dimension-less, and can be directly compared to other panels. The lower plot in each panel shows the fractional difference of each profile relative to the best-fit NFW profile. The other three panels show the lensing profiles for the same halos when implementing the NFW scaling analysis for each halo or for the stacked analysis (Eq. 15). Note that the same color curves in the different panels correspond to the same halo. *Upper-right panel*: The lensing profile when using the NFW parameters of three-dimensional mass profile for each halo, $(M_{500c}^{\mathrm{3D\,NFW-fit}}, c_{500c}^{\mathrm{3D\,NFW-fit}})$, in the NFW scaling analysis. *Lower-left panel*: The results when using the NFW parameters of two-dimensional lensing distortion profile, $(M_{500c}^{\mathrm{2D\,NFW-fit}}, c_{500c}^{\mathrm{2D\,NFW-fit}})$. *Lower-right panel*: Similar to the upper-right panel, but using the best-fit halo mass of each halo and using the halo concentration inferred from the scaling relation, $c_\Delta = c_\Delta(M_\Delta; z)$ in DK15. In these three panels, the blue curve is not a fit, but rather the NFW prediction itself, $f^{\mathrm{NFW}}(x)$ (Eq. 5), where we included the reduced shear correction from the best-fit NFW model to the stacked lensing profile in the upper-left panel. Note that, for all the results, we ignored effects of measurement errors such as intrinsic ellipticities of background galaxies.

ing implementation. The lensing profiles of individual halos or the stacked lensing profile are estimated by summing the "scaled" amplitude of lensing distortion in each of the "scaled" radial bin relative to the NFW predictions of each halo (see Eq. 15). The different panels are the results when using the best-fit NFW parameters of 3D mass density profile for each halo, the NFW parameters of 2D lensing profile, or the halo mass of 3D profile, but using the concentration parameter inferred from the scaling relation, $c_{500c} = c(M_{500c})$ in DR14, respectively[6]. The lower-right panel is closest to our main results using the Subaru and X-ray data. All the three panels clearly show that the NFW scaling significantly reduces the scatters of individual lensing profiles relative to the NFW prediction, compared to the standard lensing analysis (the upper-left panel). The scatters appear to be smallest when using the best-fit NFW parameters of the 2D lensing profile. Comparing the upper-right and lower-right panels clarifies how the scatters are enlarged due to the lack of halo concentration knowledge on individual halo or shows the degradation by ignoring the intrinsic scatters of halo concentration in different halos. Encouragingly the figure shows that, even without knowledge on the concentration of each halo, the NFW scaling can reduce the scatters compared to the upper-left panel. However it should be noted that the stacked lensing profile shows a sizable deviation from the NFW profile (the blue solid curve), compared to the upper-left panel. In summary these results justify our approach of using the scatters of individual lensing profiles in order to test the universality of mass density profile in 50 clusters.

3. APPLICATION

In this section we apply, as a proof of concept, the method developed in the preceding section to the Subaru data for a sample of 50 massive clusters.

3.1. *The cluster sample*

3.1.1. *Subaru weak lensing data*

For the weak lensing measurements, we use the shape catalog of galaxies for the 50 clusters, used in the published work of Okabe et al. (2013). This is the older version of shape catalog, derived as a part of the LoCuSS collaboration (see Okabe et al. 2010a; Martino et al. 2014, for details). In brief, the 50 cluster sample was selected from the *ROSAT* All Sky Survey catalogs (Ebeling et al. 1998, 2000; Böhringer et al. 2004) that satisfy the criteria given as $L_X[0.1 - 2.4\mathrm{keV}]/E(z)^{2.7} \geq 4.2 \times 10^{44}$ erg s^{-1}, $0.15 \leq z \leq 0.30$, $n_H < 7 \times 10^{20}$cm^{-2}, and $-25° < \delta < +65°$, where $E(z) \equiv H(z)/H_0$ is the normalized Hubble expansion rate. The criteria on the redshift range and the declination are adopted in order to have a sufficiently high elevation of these clusters from the Subaru telescope and to have an entire coverage of the virial region of these clusters with the field of view of the Subaru Suprime-Cam camera (Miyazaki et al. 2002).

All the clusters were observed by Subaru, with two passbands at least: *i* or I_C data, which was used for the weak lensing analysis in Okabe et al. (2013), and the bluer-passband data, *V* or *g* data. For this paper, we take the position of brightest cluster galaxy in each cluster as the cluster center.

---

[6] For the measurement we used the X-ray observables to infer the halo mass of each cluster. Here we assumed that the X-ray observables are sensitive to the inner region of each cluster or relatively less sensitive to the projection effect than in weak lensing. Hence we assume that the X-ray observables gives a proxy of the halo mass via the 3D profile.

Okabe et al. (2010a) carefully studied a possible miscentering effect by comparing the lensing signals of various center proxies such as the X-ray peak, and concluded that the miscentering, even if exists, should be well within 100 kpc in radius (more exactly, within about 50 kpc in our estimate), which is inside the minimum radius used in this paper.

An important systematic effect in the weak lensing measurements is a possible residual uncertainty in estimation of source galaxy redshifts, mainly limited by the two passband data alone. Okabe et al. (2013) developed a method of making a secure sample of background galaxies, which is selecting galaxies with color sufficiently redder than the red-sequence of early-type galaxies in each cluster region. In other words, they found that it is very difficult to select "blue" background galaxies from the two passband data alone or such blue galaxies always appear to be contaminated by foreground or member (therefore unlensed) galaxies. However, this selection is conservative and leaves only a small number of galaxies in the sample so as to ensure less than 1% contamination or dilution effect on the lensing signal, even if exists: the mean number density of galaxies is about 5 arcmin^{-2}, a factor 4 or 5 smaller than the number density of all the galaxies for which weak lensing analysis is usable in the original *i*- or I_c-band catalog. Hence the measurement errors of weak lensing signals are dominated by the shape noise, which justifies that we ignore the error contribution of projection effects due to different structures along the same line-of-sight to the cluster. The mean redshift of background galaxies in each cluster was estimated by matching color of the selected background galaxies to the COSMOS catalog. Since all the clusters are at low redshift $z \sim 0.2$ and the deep Subaru data typically probe galaxies at $z \sim 0.8$, the lensing efficiency has a weak dependence on source redshift and a possible residual uncertainty in the source redshift would not be large and should be less than a 10% change in the lensing amplitude even if exists (see § 5.7.2 in Okabe et al. 2010a). We should also keep in mind an additional uncertainty due to the sample variance in the COSMOS calibration catalog, which refers a possible difference in the populations of source galaxies in between the COSMOS and cluster regions.

Again note that the purpose of this paper is to give a proof of concept of the novel cluster lensing measurement method, so the results we will show below is based on the catalog of Okabe et al. (2013). See Okabe et al. (2015) for the improved results of weak lensing measurements based on a more careful treatment of shape measurement and photo-*z* uncertainty.

3.1.2. *X-ray observables: hydrostatic equilibrium mass, gas mass and gas temperature*

All the 50 clusters were observed by the X-ray satellites, *XMM-Newton* or/and *Chandra* (Zhang et al. 2010; Martino et al. 2014). In this paper, we use the X-ray observables in Martino et al. (2014) to infer the halo mass for each of the 50 clusters, which was estimated based on either or both of the *XMM* and/or *Chandra* data. In the following we will use two mass estimates: the mass estimated based on the hydrostatic equilibrium assumption (hereafter HSE for simplicity) and the self-similar scaling relation of gas mass (M_{gas}) with the halo mass:

- *Hydrostatic equilibrium (HSE) mass* – Martino et al. (2014) carefully developed a method of estimating the HSE mass of each cluster by combining the surface brightness and temperature profiles, measured from the
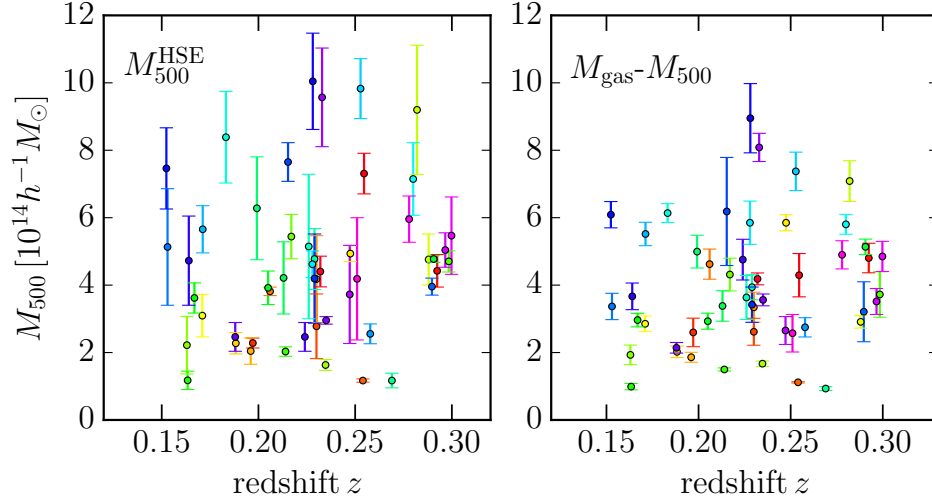
Figure 5. The 50 clusters used in this paper, in the cluster mass (M_{500c}) and redshift plane. The mass estimate of each cluster was taken from Martino et al. (2014) (see also Table 1), derived based on the *Chandra* and/or *XMM* X-ray data. The left panel is the mass estimate based on the hydrostatic equilibrium (HSE) assumption, while the right panel shows the results derived using the scaling relation of X-ray gas mass with halo mass (Eq. 22), respectively. The errorbars of each cluster are also taken from Martino et al. (2014) (for $M_{gas,500}$ we propagated the errors of gas mass). Comparing the two panels reveals that the same cluster (symbols at the same *x*-axis value) generally has different mass estimates and errorbars.

Chandra and/or *XMM* data:

$$M(< r) = -\frac{kT_g(r)r}{G\mu m_p}\left[\frac{d\ln\rho_g(r)}{d\ln r} + \frac{d\ln T_g(r)}{d\ln r}\right], \quad (21)$$

where $T_g(r)$ and $\rho_g(r)$ are the three-dimensional radial profiles of gas temperature and density, respectively. We will use the halo mass estimate for $\Delta = 500$ overdensity, M_{500c}, in Table 2 of Martino et al. (2014). For some of the clusters, the mass estimates were derived for both the *Chandra* and *XMM* data. If the two mass estimates are available, we use the *XMM*-derived mass because the mass accuracy is better than that of the *Chandra*-based estimate. Note that the two estimates are consistent with each other within the errorbars, We use the *XMM*-based mass for 32 clusters, and use the *Chandra*-based mass for the remaining 18 clusters.

- M_{gas} *derived mass* – The direct X-ray observables are the gas mass and temperature. If non-gravitational processes are not significant for cluster evolution, the mass, temperature, size and other properties of galaxy cluster follow self-similar scaling relations (Kaiser 1986). The ratio of the total matter and gas masses in a cluster region is expected to follow the scaling relation: $M_\Delta(< r) \propto M_{gas,\Delta}(< r)$. For the interior gas mass, we will use the $M_{gas,500}$ value in Table 3 of Martino et al. (2014) for each cluster. For the normalization factor, we here simply employ the cosmic mean value that is inferred from the latest Planck result (Planck Collaboration et al. 2015):

$$\frac{M_{500c}}{10^{14}M_\odot} = \frac{\Omega_{m0}}{\Omega_{b0}}\frac{M_{gas,500}}{10^{14}M_\odot}$$

$$\simeq 11.6 \times \left(\frac{M_{gas,500}}{10^{14}h^{-3/2}M_\odot}\right), \quad (22)$$

where we took the best-fit values of $\Omega_{b0}h^2$, $\Omega_{m0}h^2$ and h in Table 3 of Planck Collaboration et al. (2015) to compute the normalization constant. The unit $h^{-3/2}$ of gas

mass is from the fact that the gas mass estimate from X-ray observables has the *h*-dependence. Note that the overdensity radius r_{500c} used for the interior mass definition is from the total mass profile derived from the HSE assumption, Eq. (21). In this sense, exactly speaking, this treatment is not self-consistent. Comparing the above normalization constant with Figure 2 in Okabe et al. (2014) shows that our model is within a range of the normalization constants implied from observations. However, a precise determination of the normalization constant is not our primary purpose, and the above choice can be considered as a working example. We will below study how variations in the above scaling relation change the weak lensing measurements with NFW scaling.

Table 1 gives a summary of the above X-ray observables: the HSE mass and the gas mass for each. Figure 5 shows the distribution of 50 clusters in the plane of halo mass and redshift. The two proxies give a different estimate of halo mass on individual cluster basis and the errorbars quoted are also different. The mean mass of 50 clusters (without lensing weights), $\langle M_{500c}\rangle /[10^{14}h^{-1}M_\odot] = 4.42$ or 3.82 for the HSE or gas mass proxy, respectively.

3.2. *The stacked lensing analysis of 50 clusters with and without NFW scaling*

First of all, in Figure 6, we show the stacked lensing profile of 50 clusters, without NFW scaling, for the sake of comparison with the following results. This result reproduces Figure 3 in Okabe et al. (2013). We employed 32 logarithmically-spaced bins over the radial range of $0.14 \leq R/[h^{-1}\text{Mpc}] \leq 2.8$. As given by Eq. (12), we estimated the representative value of each radial bin by averaging the centric-radii of background galaxies in the annulus, and therefore the neighboring bins are, exactly speaking, not equally spaced, although the difference is very small after the average of 50 clusters. The cumulative signal-to-noise ratio is significant: $S/N \simeq 34.5$. From the fitting to an NFW profile, we find the best-fit parameters, $M_{500c} = (4.0\pm0.1)\times10^{14}h^{-1}M_\odot$ and $c_{500c} = 2.8\pm0.3$, re-

Table 1
X-ray and Lensing Observables of 50 Clusters

Cluster	redshift	X-ray data			M_{500c} $[10^{14} M_\odot]$		Lensing observables		
		r_{500c} [Mpc]	Telescope	$M_{\mathrm{gas,500}}$ $[10^{14} M_\odot]$	M_{500c}^{HSE}	$M_{500c}^{M_{\mathrm{gas}}}$	$(S/N)_{\mathrm{WL}}$	$(d^2)^{\mathrm{HSE}}$	$(d^2)^{M_{\mathrm{gas}}}$
A2697	0.232	1.20 ± 0.04	*XMM*	0.880 ± 0.037	6.29 ± 0.65	5.98 ± 0.25	6.42	4.47	4.62
A68	0.255	1.40 ± 0.20	*XMM*	0.903 ± 0.135	10.44 ± 0.86	6.13 ± 0.92	6.24	13.62	7.52
A2813	0.292	1.25 ± 0.10	*XMM*	1.010 ± 0.092	6.32 ± 0.69	6.86 ± 0.63	5.45	4.66	4.28
A115	0.197	0.89 ± 0.07	*XMM*	0.546 ± 0.089	3.26 ± 0.21	3.71 ± 0.60	3.61	8.20	8.46
A141	0.230	1.02 ± 0.12	*Chandra*	0.550 ± 0.084	3.97 ± 1.37	3.74 ± 0.58	5.35	6.01	6.36
ZwCl0104	0.254	0.76 ± 0.01	*Chandra*	0.235 ± 0.004	1.67 ± 0.07	1.60 ± 0.03	3.55	5.46	5.50
A209	0.206	1.15 ± 0.07	*XMM*	0.972 ± 0.094	5.45 ± 0.18	6.60 ± 0.64	9.14	21.84	17.37
A267	0.230	1.17 ± 0.12	*Chandra*	0.703 ± 0.094	5.97 ± 1.84	4.78 ± 0.64	5.37	7.01	7.47
A291	0.196	0.94 ± 0.06	*XMM*	0.391 ± 0.031	2.92 ± 0.56	2.66 ± 0.21	4.92	8.61	8.92
A383	0.188	1.01 ± 0.08	*XMM*	0.425 ± 0.036	3.25 ± 0.45	2.89 ± 0.24	5.74	9.11	9.80
A521	0.248	1.25 ± 0.04	*XMM*	1.230 ± 0.050	7.05 ± 0.34	8.36 ± 0.34	5.98	4.66	5.23
A586	0.171	1.09 ± 0.08	*Chandra*	0.600 ± 0.049	4.42 ± 0.90	4.08 ± 0.33	5.58	10.90	11.47
A611	0.288	1.20 ± 0.06	*Chandra*	0.612 ± 0.039	6.80 ± 1.08	4.16 ± 0.26	5.98	8.24	12.30
A697	0.282	1.50 ± 0.10	*Chandra*	1.490 ± 0.127	13.14 ± 2.74	10.12 ± 0.86	4.89	20.89	12.84
ZwCl0857	0.235	0.85 ± 0.04	*XMM*	0.351 ± 0.017	2.33 ± 0.23	2.38 ± 0.12	2.45	4.53	4.60
A750	0.163	0.97 ± 0.12	*Chandra*	0.406 ± 0.061	3.17 ± 1.22	2.76 ± 0.41	6.82	16.54	18.17
A773	0.217	1.21 ± 0.11	*XMM*	0.907 ± 0.102	7.77 ± 0.94	6.16 ± 0.69	9.03	7.40	11.40
A781	0.298	1.13 ± 0.17	*XMM*	0.783 ± 0.142	6.72 ± 0.45	5.32 ± 0.96	4.27	28.93	25.32
ZwCl0949	0.214	0.93 ± 0.02	*Chandra*	0.315 ± 0.010	2.90 ± 0.20	2.14 ± 0.07	5.50	15.34	16.79
A901	0.163	0.79 ± 0.06	*XMM*	0.208 ± 0.020	1.68 ± 0.39	1.41 ± 0.14	5.58	11.98	13.43
A907	0.167	1.08 ± 0.06	*XMM*	0.623 ± 0.042	5.17 ± 0.64	4.23 ± 0.29	7.71	11.32	14.53
A963	0.205	1.14 ± 0.07	*XMM*	0.616 ± 0.050	5.60 ± 0.71	4.18 ± 0.34	7.49	13.40	17.46
ZwCl1021	0.291	1.26 ± 0.05	*XMM*	1.080 ± 0.048	6.82 ± 0.14	7.34 ± 0.33	6.78	8.76	9.23
A1423	0.213	1.18 ± 0.10	*Chandra*	0.711 ± 0.095	6.02 ± 1.53	4.83 ± 0.65	4.58	9.89	6.95
A1451	0.199	1.36 ± 0.11	*XMM*	1.050 ± 0.102	8.97 ± 2.18	7.13 ± 0.69	8.25	6.30	5.44
RXCJ1212	0.269	0.76 ± 0.05	*XMM*	0.196 ± 0.012	1.67 ± 0.31	1.33 ± 0.08	3.00	9.34	8.86
ZwCl1231	0.229	1.23 ± 0.08	*Chandra*	0.828 ± 0.078	6.82 ± 1.29	5.63 ± 0.53	5.09	17.35	16.05
A1682	0.226	1.24 ± 0.18	*Chandra*	0.764 ± 0.137	7.35 ± 3.06	5.19 ± 0.93	7.30	6.12	8.03
A1689	0.183	1.52 ± 0.07	*XMM*	1.290 ± 0.059	11.98 ± 1.94	8.76 ± 0.40	9.42	11.25	16.82
A1758N	0.280	1.38 ± 0.07	*Chandra*	1.220 ± 0.062	10.21 ± 1.54	8.29 ± 0.42	3.10	13.65	10.03
A1763	0.228	1.33 ± 0.11	*XMM*	1.230 ± 0.135	6.60 ± 0.56	8.36 ± 0.92	6.75	9.58	7.09
A1835	0.253	1.57 ± 0.11	*XMM*	1.550 ± 0.120	14.04 ± 1.27	10.53 ± 0.82	5.96	14.77	13.27
A1914	0.171	1.38 ± 0.08	*XMM*	1.160 ± 0.073	8.08 ± 1.00	7.88 ± 0.50	4.83	9.22	8.88
ZwCl1454	0.258	1.06 ± 0.10	*XMM*	0.578 ± 0.060	3.65 ± 0.42	3.93 ± 0.41	3.18	3.94	4.13
A2009	0.153	1.29 ± 0.13	*Chandra*	0.708 ± 0.082	7.33 ± 2.47	4.81 ± 0.56	4.91	5.79	5.14
ZwCl1459	0.290	1.08 ± 0.25	*XMM*	0.675 ± 0.187	5.65 ± 0.36	4.59 ± 1.27	3.31	4.16	3.73
RXCJ1504	0.215	1.47 ± 0.35	*XMM*	1.300 ± 0.337	10.93 ± 0.82	8.83 ± 2.29	4.55	7.70	6.23
A2111	0.229	1.17 ± 0.14	*Chandra*	0.719 ± 0.110	5.99 ± 1.89	4.88 ± 0.75	4.83	13.10	12.57
A2204	0.152	1.49 ± 0.08	*XMM*	1.280 ± 0.082	10.66 ± 1.72	8.70 ± 0.56	6.48	11.20	9.16
A2219	0.228	1.75 ± 0.11	*XMM*	1.882 ± 0.216	14.35 ± 2.04	12.79 ± 1.47	7.51	6.21	6.06
RXCJ1720	0.164	1.23 ± 0.11	*XMM*	0.771 ± 0.083	6.97 ± 0.68	5.24 ± 0.56	3.80	11.47	7.02
A2261	0.224	1.22 ± 0.12	*Chandra*	1.000 ± 0.127	6.75 ± 1.89	6.79 ± 0.86	8.88	13.44	13.33
RXCJ2102	0.188	1.00 ± 0.06	*XMM*	0.450 ± 0.033	3.52 ± 0.61	3.06 ± 0.22	4.04	13.87	12.78
RXJ2129	0.235	1.08 ± 0.04	*XMM*	0.749 ± 0.037	4.22 ± 0.16	5.09 ± 0.25	3.17	5.10	6.17
A2390	0.233	1.60 ± 0.11	*XMM*	1.700 ± 0.088	13.67 ± 2.09	11.55 ± 0.60	6.30	8.47	7.41
A2485	0.247	1.11 ± 0.15	*Chandra*	0.558 ± 0.087	5.32 ± 2.08	3.79 ± 0.59	4.71	1.89	0.52
A2537	0.297	1.19 ± 0.10	*XMM*	0.739 ± 0.081	7.20 ± 0.73	5.02 ± 0.55	5.05	8.73	9.81
A2552	0.300	1.25 ± 0.09	*Chandra*	1.020 ± 0.094	7.81 ± 1.64	6.93 ± 0.64	3.98	11.30	10.85
A2631	0.278	1.20 ± 0.09	*XMM*	1.030 ± 0.088	8.51 ± 0.98	6.93 ± 0.64	4.61	18.05	16.23
A2645	0.251	1.15 ± 0.18	*Chandra*	0.541 ± 0.117	5.98 ± 2.59	3.68 ± 0.79	6.59	19.54	19.62

Note. — The X-ray observables (r_{500c}, M_{500c}^{HSE} and $M_{\mathrm{gas,500}}$) taken from Tables 2 and 3 of Martino et al. (2014): r_{500c} is the radius for the interior overdensity $\Delta = 500$, M_{500c}^{HSE} is the mass estimate based on the hydrostatic equilibrium, and $M_{\mathrm{gas,500}}$ is the gas mass interior to r_{500} (see text for details). $M_{500c}^{M_{\mathrm{gas}}}$ is the total mass interior to r_{500c} assuming the *simple* self-similar scaling relation given by Eq. (22). The mean mass of 50 clusters $\langle M_{500c}\rangle /[10^{14} h^{-1} M_\odot] = 4.42$ or 3.82 for the HSE and gas mass cases, respectively. The last three columns are the lensing observables that are computed from the lensing measurement of Okabe et al. (2013). $(S/N)_{\mathrm{WL}}$ is the total signal-to-noise ratio of lensing distortion measurement for each cluster over the 8 radial bins in the range $0.14 \le R/[h^{-1}\mathrm{Mpc}] \le 2.8$. $(d^2)^{\mathrm{HSE}}$ or $(d^2)^{M_{\mathrm{gas}}}$ is the deviation of the lensing distortion profile compared to the NFW prediction, defined by Eq. (17) or (18) for each cluster.
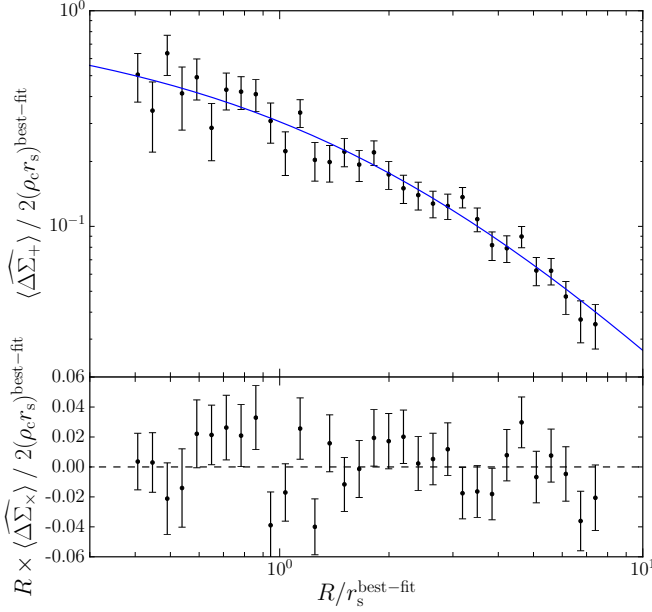
Figure 6. *Upper panel*: The stacked distortion profile measured from 50 Subaru clusters, based on the standard stacked lensing analysis (Eq. 9), i.e. without NFW scaling implementation. We employed the 32 logarithmically-spaced bins over a fixed range of radii, $0.14 \leq R/[h^{-1}\mathrm{Mpc}] < 2.8$, for all the 50 clusters. The errorbar at each bin is computed from Eq. (13) assuming that the statistical noise is dominated by the intrinsic ellipticities of background galaxies. The solid curve is the best-fit NFW model, which is specified by the best-fit parameters $M_{500c} = (4.0 \pm 0.1) \times 10^{14} h^{-1} M_\odot$ and $c_{500c} = 2.8 \pm 0.3$. The best-fit model reproduces the results in Okabe et al. (2013) within the errorbars[a]. For the sake of comparison with the following figures, we plot the distortion profile relative to the best-fit NFW model, as a function of the radius relative to the scale radius of the best-fit NFW model. Note that the representative value of each radial bin is estimated from the average of radii of background galaxies that reside in the annulus (see Eq. 12). The reduced chi-square for the best-fit model is $\chi^2/\mathrm{d.o.f} = 22.5/(32-2)$. *Lower panel*: Similar to the above panel, but for the $45°$-rotated components of background galaxy ellipticities.

[a]Okabe et al. (2013) used the physical coordinates in the stacking analysis, and this leads to a slight change in the best-fit NFW parameters.

spectively. The reduced chi-square is $\chi^2/\mathrm{d.o.f} = 22.5/(32-2)$. Thus the results show that, even if the X-ray inferred masses differ from each other by up to a factor of 10, the stacked profile is so remarkably well fitted by the NFW model. This appears to be consistent with what we found from the test using the simulated halos in Figure 4.

We now move to the main results of this paper. We employ the following procedures to implement the NFW scaling analysis of weak lensing measurements:

(1) *NFW scaling of galaxy ellipticities and radial bins* – First, we employ, for the a-th cluster ($a = 1, 2, \cdots, 50$), the halo mass inferred from the X-ray observables, either HSE or gas mass (see § 3.1.2). We then use the c-M relation in DK15 to infer the halo concentration for the cluster. Using the X-ray inferred parameters, $M^{\mathrm{X}}_{500(a)}$ and $c^{\mathrm{X}}_{500(a)}$, we compute the expected lensing amplitude and the NFW scale-radius, $2[\rho_c r_s]_{(a)}$ and $r_{s(a)}$, respectively, in order to "scale" the amplitude of galaxy ellipticities as well as the radius for the s_a-th background galaxy in the a-th cluster region: $e_{+(s_a)} \rightarrow e_{+(s_a)}/[2\rho_c r_s]_{(a)}$ and $R_{(a)s_a} \rightarrow x = R_{(a)s_a}/r_{s(a)}$. Thus, even if we use the same background galaxies over a fixed range of radii, $0.14 \leq R/[h^{-1}\mathrm{Mpc}] \leq 2.8$, this NFW scaling leads to different ranges of the scaled
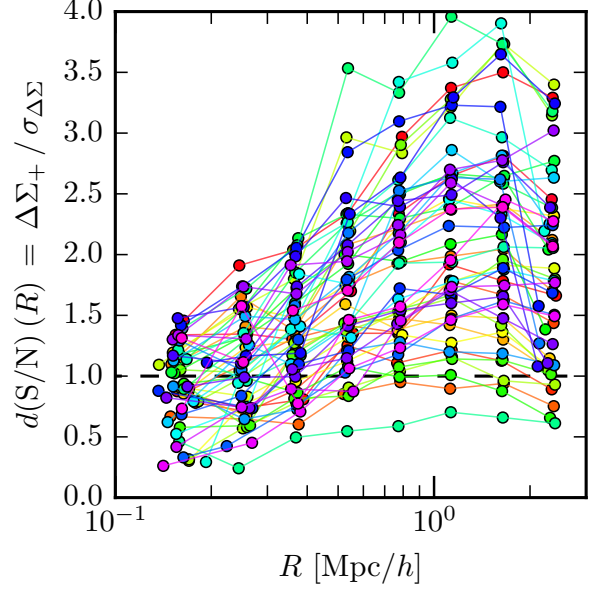

Figure 7. The expected, differential signal-to-noise ratio, $\mathrm{d}(S/N)$, at each of the 8 logarithmically-spaced radial bins in the range $0.14 \leq R/[h^{-1}\mathrm{Mpc}] \leq 2.8$, for each of 50 Subaru clusters. We computed the $\mathrm{d}(S/N)$ value as follows. For the expected signal, we used an analytical NFW profile for each cluster assuming the X-ray HSE mass and the halo concentration inferred from the $c-M$ relation in DK15. To compute the statistical noise in each bin, we used the real Subaru data of background galaxies (their distribution on the sky, the intrinsic shapes and the lensing weights) in each cluster region. Most of the data points, about 79% of 400 data points ($400 = 50 \times 8$), are expected to have the $\mathrm{d}(S/N)$ values greater than unity. The same color symbols at different radial bins correspond to the same cluster. Note that the representative value of each radial bin is computed from Eq. (12) taking into account the radii and weights of background galaxies, which causes variations in the representative values especially for the small radii, even if we work on the fixed range of $0.14 \leq R/[h^{-1}\mathrm{Mpc}] \leq 2.8$.

radii, x, for different clusters. The different amount of radial scaling requires a careful treatment of the radial binning, especially when comparing the lensing distortion profiles with and without NFW scaling. In the following we use the different binning schemes depending on either case studying the stacked lensing profile or studying the scatters of 50 cluster lensing profiles relative to the NFW prediction, which are summarized by the procedures (2a) and (2b) below.

(2a) *Stacked lensing analysis with NFW scaling implementation* – As in Figure 6, we will study the stacked distortion profile of 50 clusters after the NFW scaling of each cluster. Similarly to Figure 6, we will use the 32 logarithmically-spaced bins in the "scaled" radius, x, where we used exactly the same background galaxies behind the 50 clusters. After stacking 50 clusters, we can expect a significant detection of the lensing signal at each radial bin, as implied from Figure 6. However, the above NFW scaling transforms the original radial range to a different range of the scaled radius x for each cluster. Hence, the sample of background galaxies in each bin of R or x radii differ from each other. Nevertheless, since the stacked lensing has a sufficiently high S/N at each bin, we checked that the NFW scaling almost conserves the total S/N value (exactly speaking, it causes only about 0.5% fractional change). We estimate the representative value of each radial bin in a
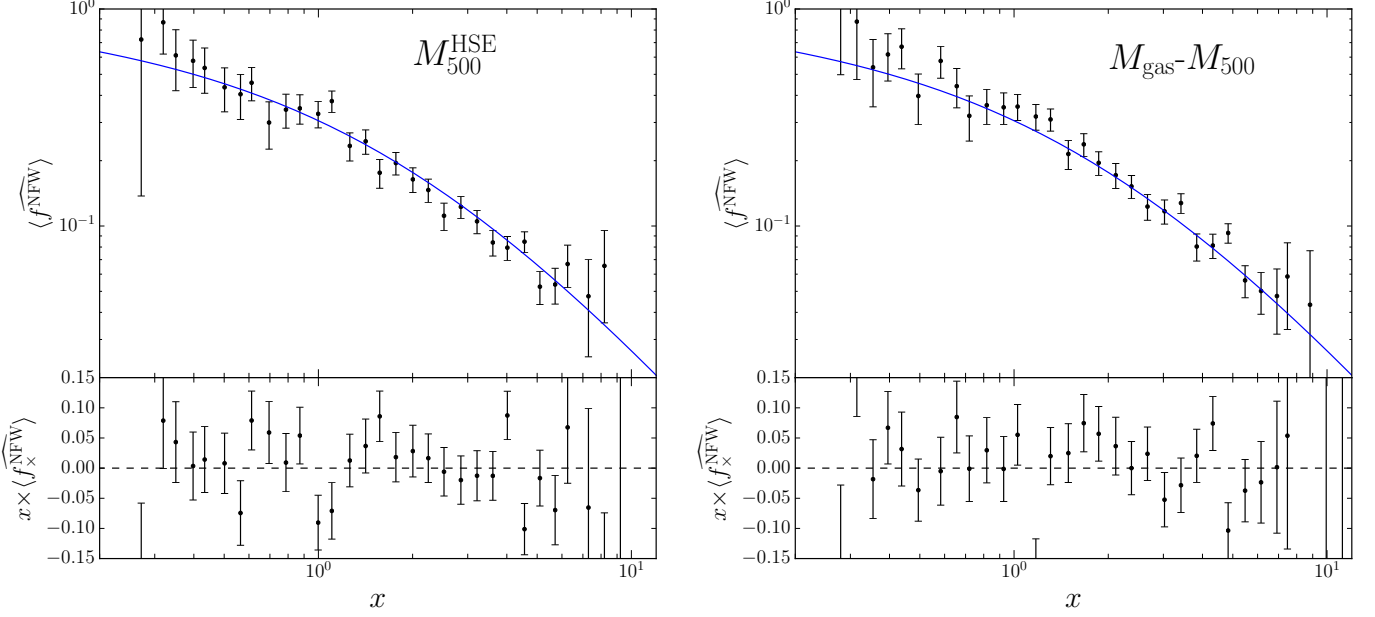
Figure 8. Similar to Figure 6, but the stacked distortion profile of 50 clusters when implementing the NFW scaling analysis: we summed the "scaled" amplitudes of background galaxy ellipticities in each bin of the "scaled" radii according to the NFW parameters, halo mass and concentration, inferred for each cluster based on its X-ray observables. In the left or right panels, we employed the X-ray inferred mass of each cluster from the hydrostatic equilibrium assumption (HSE) or the gas mass, respectively, and then used the halo concentration inferred from the scaling relation $c = c(M; z)$ in DK15. Note that we used exactly the same background galaxies as those for the analysis without NFW scaling in Figure 6. The errorbar at each bin is computed based on Eq. (16). The solid curve in each panel is *not* a fit, but the NFW prediction (f^{NFW} given by Eq. 5) including a small correction due to reduced shear at the small radii (see below Eq. 15 for details). The reduced chi-square is $\chi^2/\mathrm{d.o.f} = 31.3/32$ or $30.7/32$ for the HSE or gas mass case, respectively.
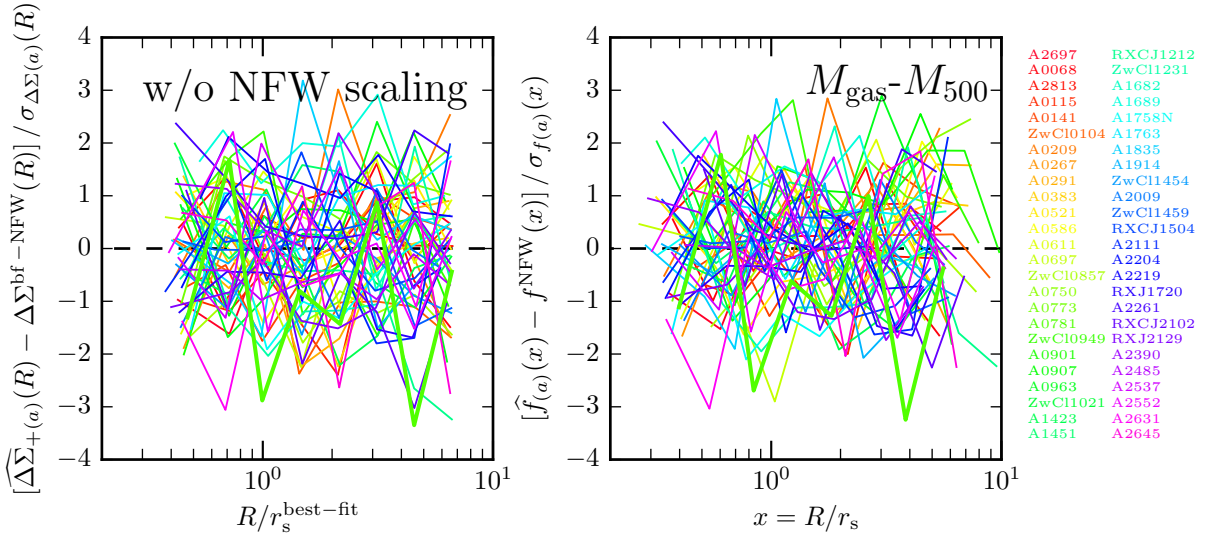
Figure 9. The difference between the lensing distortion profiles of 50 clusters and the best-fit NFW profile ($\Delta\Sigma^{\mathrm{best-fit}}(R)$) or the normalized NFW profile ($f^{\mathrm{NFW}}(x)$) for the weak lensing analysis with or without NFW scaling implementation in the left or right panel, respectively, as in the lower panels of Figure 4. Here we show in the right panel the result when using the gas mass to estimate the halo mass of each cluster, as in the right panel of Figure 8. To make a fair comparison, we show the relative difference to the statistical error at each radial bin (see Eqs. 17 and 18). Since the lensing profile is noisy on individual cluster basis due to the fewer number of background galaxies, we employed the 8 logarithmically-spaced bins in the fixed range of $0.14 \leq R/[h^{-1}\mathrm{Mpc}] \leq 2.8$ for all the clusters as in Figure 7. In addition, we used the same background galaxies in each radial bin before and after the NFW scaling transformation, $x = R/r_s$, for each cluster so that the differences become identical if we set the model NFW profile $\Delta\Sigma^{\mathrm{bf-NFW}} = f^{\mathrm{NFW}} = 0$ (see the procedure 2b in § 3.2 for details). Also note that, due to the NFW scaling, the fixed radial range in the left panel is transformed to the different range of the scaled radius for different clusters. The same-color curves in the two panels correspond to the same cluster, and the bold curve shows, as an example, the result for A781, which has the largest deviation from the NFW profile. Since the sum of squares of all the curves gives an estimate to quantify the scatters of 50 cluster lensing profiles relative to the NFW model – we call the d^2 value. The NFW scaling yields $d^2 = 527.1$ or 504.6 for the HSE and gas mass cases, respectively, compared to $d^2 = 543.2$ for the case without NFW scaling (Figure 6). This corresponds to the improvement $\Delta d^2 = d^2 - d^2_{\mathrm{w-scaling}} = (4.0)^2$ or $(6.2)^2$, respectively.
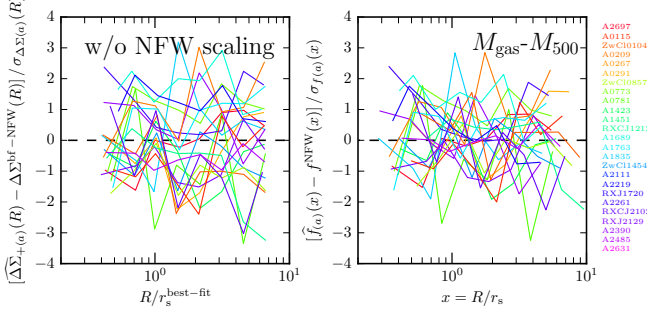
Figure 10. Similar to the previous figure, but the scatters for 25 clusters, which are a half of 50 clusters that have the larger value of Δd^2 (Eq. 23) than other 25 clusters on individual cluster basis. Comparing the left and right panels more clearly shows that the NFW scaling reduces scatters of the lensing profiles. The cumulative value of Δd^2 for 25 clusters, $\Delta d^2 \simeq (9.3)^2$.

similar manner to Eq. (12).

(2b) *Studying the scatters of lensing profiles for 50 clusters* – As we discussed in § 2.3, we monitor the scatters of 50 cluster lensing profiles relative to the NFW prediction in order to address the existence of the universal NFW profile. To quantify the scatters, we compute the d^2 value for either case with or without NFW scaling (see Eqs. 17 and 18 for the definition). In doing this, we need to probe the "shape" of lensing profile for each cluster, and in other words each radial bin needs to be in the signal dominated regime on an individual cluster basis. Hence, if we take the 32 bins as in the stacked lensing analysis, each radial bin suffers from the shape noise contamination due to too low number density of background galaxies in each bin. To tackle this obstacle, we employ 8 logarithmically-spaced bins in the range $0.14 \leq R/[h^{-1}\mathrm{Mpc}] \leq 2.8$ for each cluster. Figure 7 shows the expected S/N at each radial bin for the 50 clusters. The figure shows that 319 data points among 400 points, corresponding to 79% of 400 data points, are expected to have the S/N value greater than unity. Hence the 8 bins seem suitable for our purpose. Table 1 gives the total S/N of each cluster when employing the 8 bins. However, the expected lensing signal at each radial bin would be still noisy. To avoid any artifact arising from the noise dominated bins, we transform each of the original bins in R to the corresponding bin in the scaled radius x after the NFW scaling, rather than redefining the radial bins for a fixed range of x. With this binning, each radial bin before and after the NFW transformation preserves the same background galaxies. Hence, this binning method preserves the S/N value in each radial bin as well as the total S/N value for each cluster, before and after the NFW scaling, as can be found from Eqs. (17) and (18) mathematically. As a result, the different clusters cover different ranges of the scaled radius x.

Figure 8 shows the stacked lensing profiles after implementing the NFW scaling (the above case 2a), using the halo mass proxies based on the HSE assumption or the gas mass, respectively. We again note that, to have a fair comparison with Figure 6, we have used exactly the same background galaxies. The solid curve in each panel is *not* a fit, but rather is the NFW prediction (Eq. 5), including the reduced shear correction $1/[1 - \kappa^{\mathrm{NFW}}(x)]$, where we used the best-fit NFW
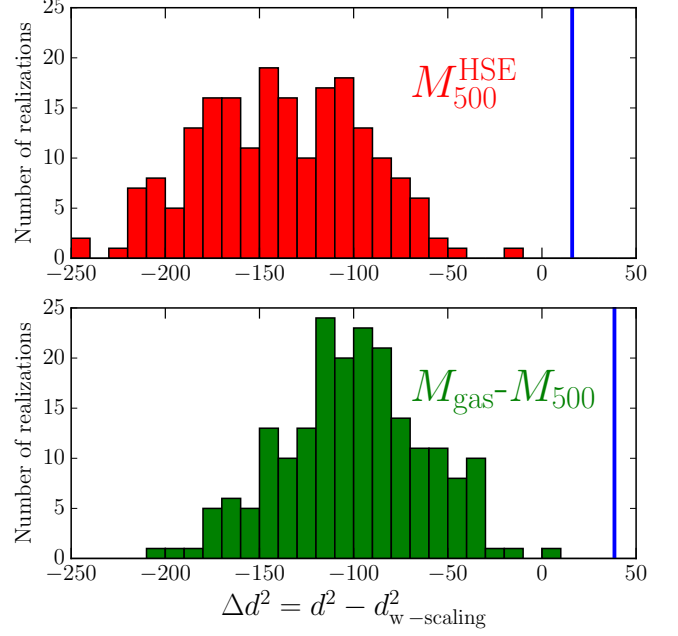

Figure 11. A test of the performance of the NFW scaling analysis in Figure 8. We randomly assigned the X-ray inferred mass to each cluster, redid the scaling analysis, and then computed the d^2 difference (Eq. 23). The histogram shows the distribution of 200 random realizations, which can be compared to our main result shown by the vertical line for either the HSE mass or the gas mass case in the upper or lower panels, respectively. All the random realizations give a negative value of Δd^2, and any of those does not reproduce the measurement value. Compared to the mean and variance of the random realizations, the measured Δd^2 value is away from the mean at 3.6 and 3.7σ for the HSE and gas mass cases, respectively.

model to the stacked distortion profile in Figure 6. The reduced shear correction is not large (by up to 20% in the amplitude at the inner bins) over the range of radii, as can be found from Figure 1. The figure shows that the stacked profile is in excellent agreement with the NFW prediction, to within the errorbars. This agreement supports the existence of NFW profile in the clusters, and implies that the X-ray inferred mass indeed gives a proxy of the genuine mass for each cluster. To be more precise, the reduced chi-square is $\chi^2/\mathrm{d.o.f} = 31.3/32$ or $30.7/32$ for the HSE or gas mass case, respectively, compared to $\chi^2/\mathrm{d.o.f} = 22.5/(32 - 2)$ in Figure 6.

Now we compare the scatters of 50 cluster lensing profiles with and without implementation the NFW scaling, quantified by the d^2 value (Eqs. 17 and 18), in order to address the existence of *universal* NFW profile. By using the above method (2b), we find the difference between the d^2 values with and without NFW scaling as

$$\Delta d^2 \equiv d^2 - d^2_{\mathrm{w-scaling}}$$
$$= \begin{cases} 543.2 - 527.1 \simeq (4.0)^2, & (\mathrm{HSE}) \\ 543.2 - 504.6 \simeq (6.2)^2, & (M_{\mathrm{gas}}\text{-}M_{500c}) \end{cases} \quad (23)$$

Thus the NFW scaling for both the HSE and gas mass cases leads to the smaller d^2-values, meaning the smaller scatters of lensing profiles relative to the NFW profile than the scatters without NFW scaling. The smaller d^2 value for the gas mass implies that the gas mass gives a better proxy of the underlying true masses of clusters (at least the relative mass differences between different clusters). Thus the NFW scaling gives about 4- or 6-σ improvement for the HSE or gas
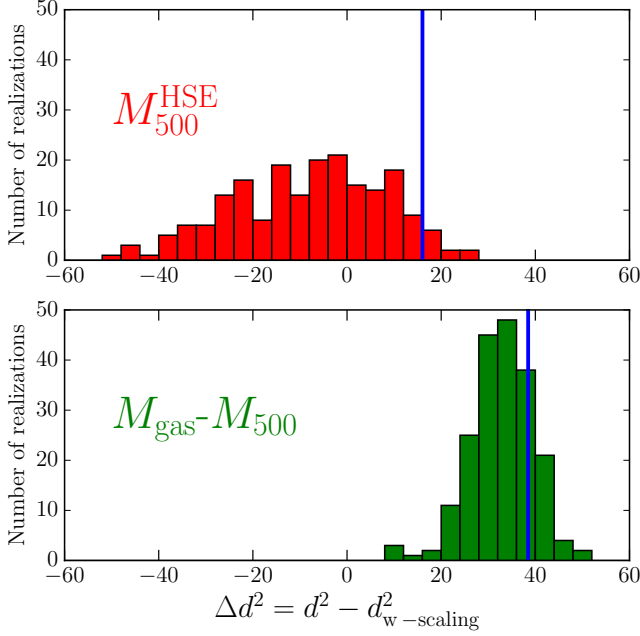
Figure 12. As in the previous figure, but show effects of the statistical errors in X-ray inferred halo mass of each cluster on the Δd^2 value. Here, we added a random scatter to each halo mass by an amount of the quoted errorbar in Table 1 assuming the Gaussian distribution, redid the weak lensing analysis with NFW scaling, and then computed the Δd^2 value for each realization.
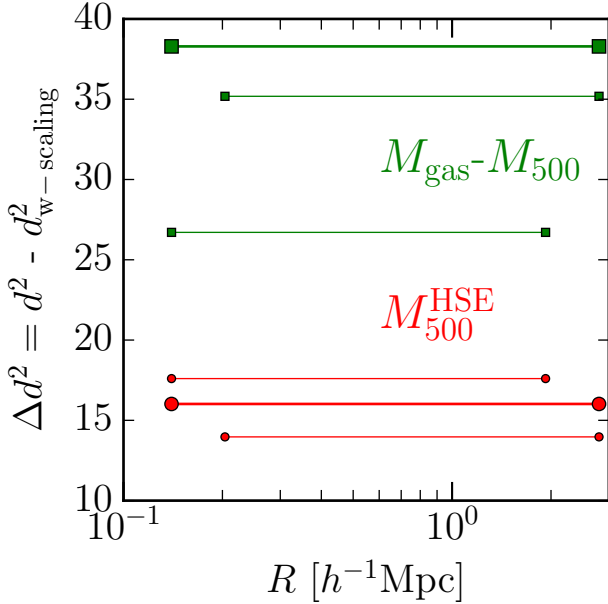

Figure 13. The figure shows the change in Δd^2 (the vertical axis) when using the different range of radii (the horizontal axis) used in the analysis. The bold lines are the results for our fiducial choice: $0.14 \leq R/[h^{-1}\mathrm{Mpc}] \leq 2.8$ and 8 logarithmically-spaced bins for all the 50 clusters. The other lines are the results when excluding the innermost or outermost bin from the analysis, respectively, for the the HSE or gas mass proxy cases, respectively.

mass, respectively, assuming that the d^2 distribution obeys a χ^2-distribution. We checked that, even if we use 16 bins instead of our fiducial 8 bins, the d^2 values themselves get enlarged because each bin is more in the shape noise dominated regime, but the d^2 difference, the Δd^2 value, is almost

unchanged.

The smaller d^2 value due to the NFW scaling arises from two parts: the scaling of lensing profile amplitude (or background galaxy ellipticities) and the scaling of cluster-centric radius. The two scalings are specified by halo mass and concentration of each cluster: $e_+/[2\rho_c r_s] \propto M_{500c}^{-1/3} c_{500c}^{-2}$ and $x = R/r_s \propto M_{500c}^{-1/3} c_{500c}$, respectively. If we include only the scaling of background galaxy ellipticities, without the radial scaling, we found $d^2_{\mathrm{w-scaling}} = 512.9$ or 526.5 for the HSE or gas mass case, which equivalently correspond to $\Delta d^2 \simeq (5.5)^2$ or $(4.1)^2$, respectively. That is, the HSE case shows an even greater improvement in Δd^2 compared to Eq. (23). On the other hand, if we include only the scaling of radius, but without the scaling of galaxy ellipticities, $d^2 = 547.1$ or 522.3, which correspond to $\Delta d^2 \simeq -3.9$ or $(4.6)^2$, respectively. Thus, for the HSE case, the radial scaling does not appear to be adequate, and rather gives a positive Δd^2. For the gas mass case, both the two scalings about equally contribute to the reduce in the d^2 value or the significance of the smaller scatters.

Figure 9 shows the contribution of each cluster to the d^2-value, which shows the argument of Eqs. (17) or (18) at each radial bin for each of 50 clusters. The total d^2 value is obtained by summing the square of each curve over the 8 radial bins and 50 clusters. Table 1 gives the total d^2-value for each cluster. The figure shows that, although it looks noisy, the NFW scaling reduces the scatters. One might notice some outlier clusters: the clusters, which have top three largest $d^2_{\mathrm{w-scaling}}$ values (see Table 1), are A781, A209, and A697 for the HSE case, while A781, A2645 and A750 for the gas mass case, respectively. For example, the bold curve denotes the A781 cluster, which is a more than 3σ outlier than the mean. The mass distribution of A781 displays three prominent peaks, indicating that the cluster is in the phase of ongoing merger (Wittman et al. 2014).

For further clarification, Figure 10 shows the scatters for 25 clusters which are a half of 50 clusters that have the larger value of Δd^2 (Eq. 23), i.e. show the better improvement of NFW scaling analysis, than other 25 clusters (see Table 1). The reduce in the scatters due to the NFW scaling is more evident. In this case, the cumulative value of Δd^2 for 25 clusters, $(\Delta d^2)^{1/2} = (86.2)^{1/2} \simeq 9.3$. Similarly, $(\Delta d^2)^{1/2} \simeq (80.6)^{1/2} \simeq 9.0$ for the HSE mass. The other 25 clusters yield smaller or even positive Δd^2 values, probably due to the complex mass distribution or the inaccuracy in X-ray inferred halo masses.

To draw a more robust conclusion, we make several tests of our results. In Figure 11, we studied how the scatters of 50 lensing profiles are enlarged if we implement the NFW scaling analysis by randomly assign the X-ray inferred halo mass to each cluster (without repeated use of X-ray mass). All the 200 random realizations have a negative value of Δd^2, and any of the random realizations cannot reproduce a similar positive value to the measured Δd^2 (the vertical line) for both the HSE and gas mass cases. To be more quantitative, the measured value Δd^2 is away at 3.6 and 3.7 σ for the two cases, respectively, compared to the mean and variance of the random realization distribution. These results give another support on the existence of NFW profile in the 50 clusters.

One important source of uncertainties in the method is a residual uncertainty in the X-ray inferred halo mass or a possible effect of intrinsic scatter in the mass scaling relation of X-ray observable. Figure 12 shows how the statistical errors

of X-ray inferred mass affect the Δd^2 value. To be more precise, we added a random scatter to halo mass of each cluster assuming the Gaussian distribution with variance given by the quoted errorbar of each X-ray mass in Table 1, i.e. $M'_{500(a)} = M^X_{500(a)} + \delta M_{(a)}$, treated the shifted mass as its true mass, and then redid the NFW scaling analysis. The figure shows that adding the random scatter to each cluster tends to decrease Δd^2, implying that the central value of the X-ray inferred mass is indeed closer to the underlying true mass. The distribution of Δd^2 is wider for the HSE mass, but this would be ascribed to the larger errors of HSE mass than those for the gas mass as can be found from Figure 5. Again encouragingly, even if adding the random errors to the gas mass, the resulting Δd^2 values are positive, supporting that the gas mass is a better proxy of the genuine cluster mass as in Figure 8.

Although we have used the fixed range of the original comoving radius, $0.14 \le R/[h^{-1}\mathrm{Mpc}] < 2.8$, for all the clusters as our fiducial choice, Figure 13 shows how the results are changed if excluding the inner- or outermost radial bin of 8 logarithmically-spaced bins from the analysis. The figure shows that, for the X-ray gas mass proxy, excluding the outer- or innermost bin degrades the NFW scaling or reduces the Δd^2 values, suggesting that the wider range of radii is important to capture the curvature of the mass profile. On the other hand, for the HSE mass case, excluding the outermost bin increases the Δd^2, again implying that the HSE mass estimate might not be as accurate to infer the genuine mass as the gas mass and involve residual systematic errors.

3.3. *Discussion and Implications*

3.3.1. *Comparison with N-body simulations*

Is the NFW scaling results in Figures 9 and Eq. (23) as expected from a viewpoint of ΛCDM structure formation model? To address this question, Figure 14 compares the measurement results and the N-body simulated halos, as in Figure 4, in a two-dimensional space of the d^2 values with and without NFW scaling. To make a fair comparison, we included the effect of intrinsic galaxy ellipticities on the simulation results. To be more precise, (1) we first populated, into each region of simulated halos, the background galaxies taken from the corresponding Subaru cluster data (matched in descending order of halo masses), (2) made a random rotation of orientation of each galaxy ellipticity, which erases the coherent lensing signal of each Subaru cluster, (3) simulated the "observed" galaxy ellipticity of each background galaxy by adding both the lensing distortion of simulated halo and the intrinsic shape, (4) performed the hypothetical lensing measurements with and without NFW scaling, and (5) computed their d^2 values, respectively. To account for the statistical variance of intrinsic ellipticities, we generated 40 realizations of the N-body simulation results: we redid the d^2 calculations after random rotation of background galaxies. For the simulation results, we consider the three cases similarly to Figure 4: the lensing analysis with NFW scaling when using the best-fit NFW parameters of 3D mass profile, the NFW parameters of 2D distortion profile, or the best-fit halo mass of 3D profile, but using the halo concentration inferred from the c-M relation, respectively. The third case is closest to what we did for the actual data. First of all, the simulation results without NFW scaling, denoted by the d^2 values in the horizontal axis, fairly well reproduce the measurements on average, reflecting that the statistical errors in the d^2 value are dominated by the shape noise. Also note that the hori-
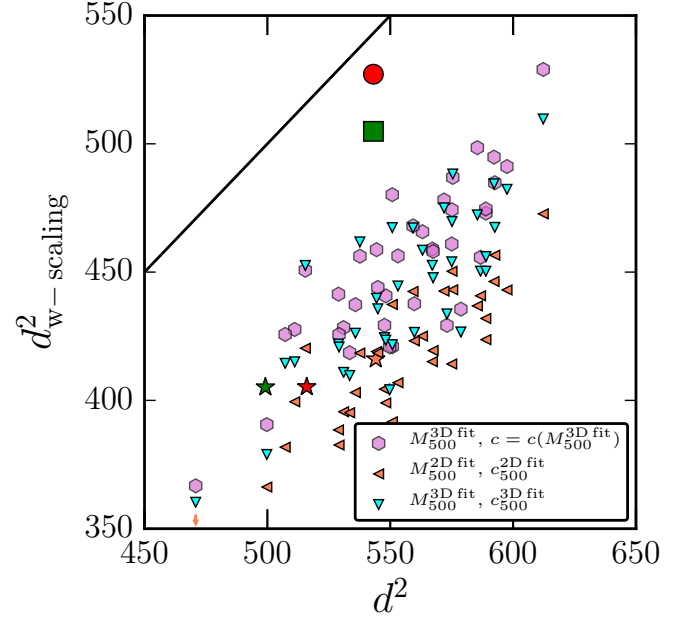

Figure 14. Comparison of the measurements and the simulation results for the d^2-values (Eqs. 17 and 18 for their definitions). The bigger-size circle and square symbols are the measurement results for the HSE and gas mass cases, respectively. The other symbols are the simulation results as in Figure 4, but including the effect of intrinsic ellipticities of background galaxies that are taken from actual Subaru data of each cluster region (see text for details). The tilted triangle and hexagon symbols are the simulation results when using the best-fit NFW parameters of 3D mass profile for each halo, the NFW parameters of 2D projected lensing profile or the best-fit mass of 3D mass profile, but the concentration inferred from the scaling relation $c_\Delta = c_\Delta(M_\Delta; z)$, respectively (see Figure 4 for details). The third case is intended to mimic what we did for the actual measurements. We show the simulation results for 40 realizations of background galaxy ellipticities. Note that, for each realization, we computed the three simulation results; each of the triangle and hexagon symbols has the same d^2 value in the horizontal axis, but different $d^2_{\mathrm{w-scaling}}$ values in the vertical axis. For comparison, the orange-color star symbol denotes one particular realization that has a similar d^2 value to the measurement for no NFW scaling case (the horizontal axis). The two star symbols in the left-lower corner are the results when using the same realization of background galaxies as in the orange-color star symbol, but using the analytical NFW profiles for the d^2 calculations. Note that the arrow in the lower-left corner denotes the simulation result that is below the plotted range.

zontal spread of the simulation realizations is roughly given by $\sqrt{d^2} \simeq \sqrt{550} \simeq 23$. However, all the simulation results with NFW scaling, $d^2_{\mathrm{w-scaling}}$ in the vertical axis, are systematically smaller than the measured values. Thus this disagreement suggests that we do not properly consider some effects inherent in the measurements on the simulation results. For comparison, the star symbols show the results when using analytical NFW halos to compute the d^2 values where we used the X-ray proxy masses for the HSE or the gas mass to compute the NFW lensing profile of each cluster. The difference between the analytical NFW halos and the simulation results is due to the complexity of mass distribution in the simulated halos, such as asphericity, substructures, and the scatters of halo concentration.

A possible source to reconcile the difference between the measurements and the simulation results in Figure 14 is an additional error or intrinsic scatter in the X-ray inferred halo mass (Stanek et al. 2010; Okabe et al. 2010b). Figure 15 addresses this question. The left panel shows how adding a scatter to each mass of simulated halos, parametrized by
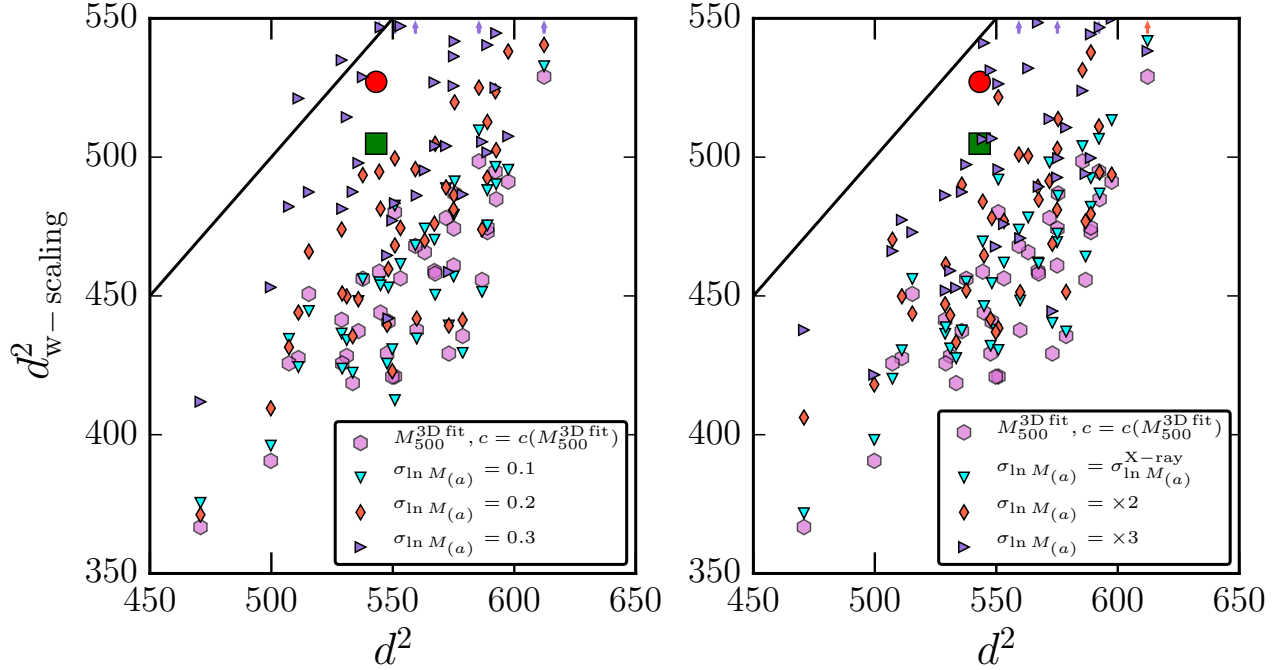
Figure 15. Similar to the previous figure, but here included the effects of mass scatter of each halo on the simulation results. The hexagon symbols are the same as in Figure 14. For each realization of background galaxies, we added a random mass scatter to each halo, simulated the lensing analysis with NFW scaling by treating the shifted mass as the true mass, and then computed the $d^2_{\rm w-scaling}$ value. Adding the halo mass scatters tends to degrade the NFW scaling results or preferentially causes an up-scatter of each simulation result in this two-dimensional space. *Left panel*: The simulation results when adding the Gaussian mass scatters by the fractional errors of $\sigma_{\ln M} = 0.1, 0.2$ or 0.3, respectively. The arrows in the upper horizontal axis denote the case that the simulation results are outside the range shown in this plot. *Right panel:* Similar to the left panel, but the results when adding a random mass scatter to each simulated cluster assuming the fractional error proportional to the quoted error of the gas mass proxy relation (assigned to the simulated halo); $\sigma_{\ln M_{(a)}} \equiv \sigma^X_{M_{(a)}}/M^X_{(a)}$ or a factor 2 or 3 bigger one.

the fractional variance $\sigma_{\ln M} = \sigma(M)/M = 0.1, 0.2$ or 0.3, degrades the $d^2_{\rm w-scaling}$ values for the NFW scaling analysis. More precisely, we randomly generated a mass scatter δM for each halo assuming the Gaussian distribution with variance $\sigma_{\ln M}$, added the scatter to each halo mass as given by $M'_{(a)} = M^{\rm 2D~fit}_{500(a)} + \delta M$, and then computed the $d^2_{\rm w-scaling}$ value by treating the shifted mass M' as the true mass of each simulated halo. For the sake of comparison, we used the same 40 realizations of background galaxies as in Figure 14, and therefore the degradation is solely due to the mass scatters. Note that, for each realization of background galaxies, adding the halo mass scatters changes only the $d^2_{\rm w-scaling}$ value in the vertical axis. The figure shows that the halo mass scatters generally degrades the NFW scaling result or equivalently enlarge the $d^2_{\rm w-scaling}$ value. However, only the additional errors of $\sigma_{\ln M} \sim 0.2$–0.3 can reproduce the measurement result for the gas mass proxy. This might imply that the X-ray halo mass involves an unknown, systematic error or intrinsic scatter.

As an alternative test, the right panel of Figure 15 shows the effects of the quoted errorbars in the X-ray inferred halo masses. Here we added a random mass scatter to each cluster, $M'_{(a)} = M^{\rm 2D~fit}_{500(a)}(1 + \delta \ln M)$ by taking the fractional mass error, $\sigma(M^X_{(a)})/M^X_{(a)}$, for each cluster (see Table 1) assuming the Gaussian distribution, and then computed the $d^2_{\rm w-scaling}$ value for each realization. Here we used the mass errors for the gas mass proxy in Table 1. Note that the mean fractional error of 50 clusters is about 0.11, but here we included variations in the errors for different clusters. The figure shows that, if each

cluster has a factor 2–3 larger mass error than the quoted error, the simulation results appear to reproduce the measurements. The mass errors of X-ray observables might underestimate the genuine mass uncertainty, perhaps due to the limitation of the X-ray based method or due to an unknown intrinsic scatter in the X-ray observable and halo mass relation (see also Okabe et al. 2010b, for the similar discussion).

3.4. *The halo mass proxy relation of X-ray observables*

The method we have so far developed involves several assumptions. For instance, to implement the lensing stacking with NFW scaling, we need to assume several scaling relations: the halo mass proxy relation of X-ray observables and the halo mass and concentration relation. In the following we address how possible variations in these scaling relations affect the NFW scaling results.

First we study a possible bias in the X-ray inferred halo mass. Since the halo mass proxy relation of X-ray gas mass showed a better performance in the NFW scaling analysis (see Eq. 23), we here consider effects of possible variations in the gas mass relation on the results. To address this, we modify Eq. (22) to parametrize the halo mass proxy relation as

$$\frac{M^X_{500}}{10^{14}M_\odot} = A \times 11.6 \times \left(\frac{M_{\rm gas}}{10^{14}h^{-3/2}M_\odot}\right)^\beta, \qquad (24)$$

where A is the normalization parameter and β is a slope parameter of the halo mass dependence. The model with $A = 1$ and $\beta = 1$ corresponds to the self-similar model given by Eq. (22). With varying the two parameters, A and β, simultaneously, we estimated the halo mass of each cluster from
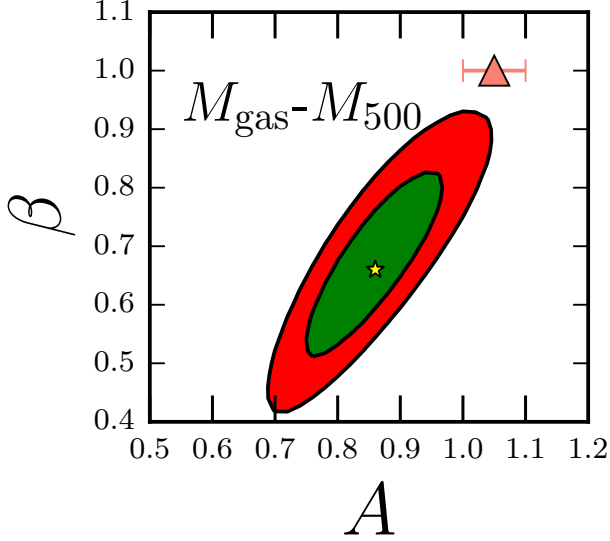
Figure 16. Effects of variations in the halo mass proxy relation of X-ray gas mass on the NFW scaling results. We model the variations as $M_{500c}/[10^{14}M_\odot] = A \times 11.6 \times (M_{\rm gas}/10^{14}h^{-3/2}M_\odot)^\beta$, where $A = 1$ and $\beta = 1$ are our fiducial model corresponding to the self-similar scaling model. We estimated the best-fit parameters (the star symbol) by minimizing the d^2 value with varying the normalization and mass slope parameters. The two contours correspond to the regions satisfying the conditions $\Delta d^2 = d^2_{\rm w-scaling}(A,\beta) - d^2_{\rm w-scaling}(A^{\rm best-fit},\beta^{\rm best-fit}) = 2.3$ or 6.17, respectively. The triangle symbol with errorbar denotes the result when varying the normalization parameter A alone, with fixing $\beta = 1$.

the X-ray gas mass based on the above proxy relation, and then redid the NFW scaling analysis. Figure 16 shows the constraint regions in the two parameter space. The best-fit parameters $A = 0.86 \pm 0.06$ and $\beta = 0.66 \pm 0.10$, which has $d^2_{\rm w-scaling} = 493.8$ compared to $d^2_{\rm min} = 504.6$ for the fiducial model as given by Eq. (23), corresponding to about 3σ improvement. Here we quoted the errorbars from the range $\Delta d^2 \leq 1$ with varying both A and β, although the degeneracy between the two parameters is significant. Thus the scatters of 50 lensing distortion profiles prefer a weaker halo mass dependence than predicted by the self-similar scaling relation at a 3σ level. Note that, if the slope parameter is fixed to $\beta = 1$, i.e. the self-scaling relation, we obtained $A = 1.05 \pm 0.05$ ($d^2_{\rm min} = 503.6$, almost no change from the fiducial model). These results might be due to some residual uncertainty in our method, and would be worth further exploring by using a larger sample of clusters or an independent mass proxy relation such as the Sunyaev-Zel'dovich effect.

3.5. *The halo mass and concentration relation*

Another important model ingredient in our analysis is the scaling relation of halo concentration with halo mass. We have so far employed the scaling relation in DK15 as for our default model. However, other works have proposed a different scaling relation from DK15. For example, Duffy et al. (2008) proposed a different fitting formula of the c-M relation, and predicts a 20–30% lower concentration than in DK15 for cluster-scale halos: more exactly $c_{200c} \sim 3$ or 4 for Duffy et al. (2008) or DK15 for cluster-scale halos of several times $10^{14}h^{-1}M_\odot$ masses at $z \sim 0$ (see Figure 9 in DK15). However, we found that, even if we use the scaling relation in Duffy et al. (2008) instead of DK15, it almost unchanges the

$d^2_{\rm w-scaling}$ value; more exactly, it enlarges the $d^2_{\rm w-scaling}$ value only by $\Delta d^2 \simeq 1$–2 for the HSE and gas mass proxy relations. Hence the current data cannot discriminate these different models of c-M relation.

Nevertheless one might ask whether or not our method allows us to constrain the underlying c-M relation. Assuming the parametrized form of c-M scaling relation given by

$$c_{500c}(M_{500c}; z) = f_c \left(\frac{M_{500c}}{4 \times 10^{14}\ h^{-1}M_\odot} \right)^{-\alpha} \times (1+z)^{-0.51}, \quad (25)$$

we minimized the $d^2_{\rm w-scaling}$ value with varying the normalization parameter and the mass slope parameter, f_c and α. Here we took the halo mass inferred from the stacked lensing in Figure 6, $M = 4 \times 10^{14}\ h^{-1}M_\odot$, for the pivot mass scale, and the redshift dependence is taken from Duffy et al. (2008)[7]. Note that we fixed the mass normalization parameter to $A = 1$ for the halo mass proxy relation of X-ray observables. Figure 17 shows that constraints on the two parameters are significantly degenerate: the $d^2_{\rm w-scaling}$ for the best-fit model is 526.3 or 503.5 for the HSE and gas mass, respectively, which is slightly smaller than our fiducial model, DK15, as found from Eq. (23). The best-fit parameters are $f_c = 2.6^{+0.3}_{-0.2}$ and $\alpha = 0.08^{0.13}_{-0.12}$ for HSE, while $f_c = 3.0 \pm 0.3$ and $\alpha = -0.08 \pm 0.18$ for the gas mass scaling relation. Thus the current data prefers the amplitude of concentration to be $c_{500c} \simeq 2.6$–3.0 for the 50 clusters of these mass scales, which is consistent with both the theory predictions in Duffy et al. (2008) and DK15 within the errorbars, but cannot well constrain the mass slope due to the limited statistics or a narrow range of halo masses.

3.6. *The halo mass profile*

The lensing analysis of NFW scaling rests on the assumption that the mass distribution in clusters follows the *universal* NFW profile. However, the NFW profile is the simplified prediction of N-body simulations, and a further improvement in our method might be available by employing a better model of the mass profile.

Several works have pointed out variations in the inner region of the mass profiles. For instance, there might be variations in the inner slope of the mass profile (e.g., see Navarro et al. 2004, and references therein). The baryonic processes would generally affect the inner structures, which tend to cause a greater mass concentration in the inner region and generally breaks the universality of the total mass profile. However, in this study, we looked into the cluster lensing signals down to $R \simeq 0.14\ h^{-1}$Mpc and above, and these effects would be unlikely to largely change our results.

Another interesting effect is a possible variation in the outer mass distribution at radii near to the virial radius or greater, as proposed in Diemer & Kravtsov (2014) and Adhikari et al. (2014). These works claimed that the logarithmic slope of massive halos steepens more sharply than the NFW predicts, at the outer regions $R \gtrsim 0.5R_{200c}$, depending on the details of mass accretion and assembly history. This breaks to some extent the universality of NFW profile at these outer radii. Note that our analysis uses the lensing profile up to $R_{\rm max} = 2.8$ Mpc/h, which corresponds to $R_{\rm max} \sim R_{200c}$ for the

---

[7] Exactly speaking the fitting formula of Duffy et al. (2008) gives the c-M relation for M_{200c}, so we converted the scaling relation to the relation between M_{500c} and c_{500c}, and found that the redshift dependence is slightly modified from the original dependence $(1+z)^{-0.47}$ by this conversion.
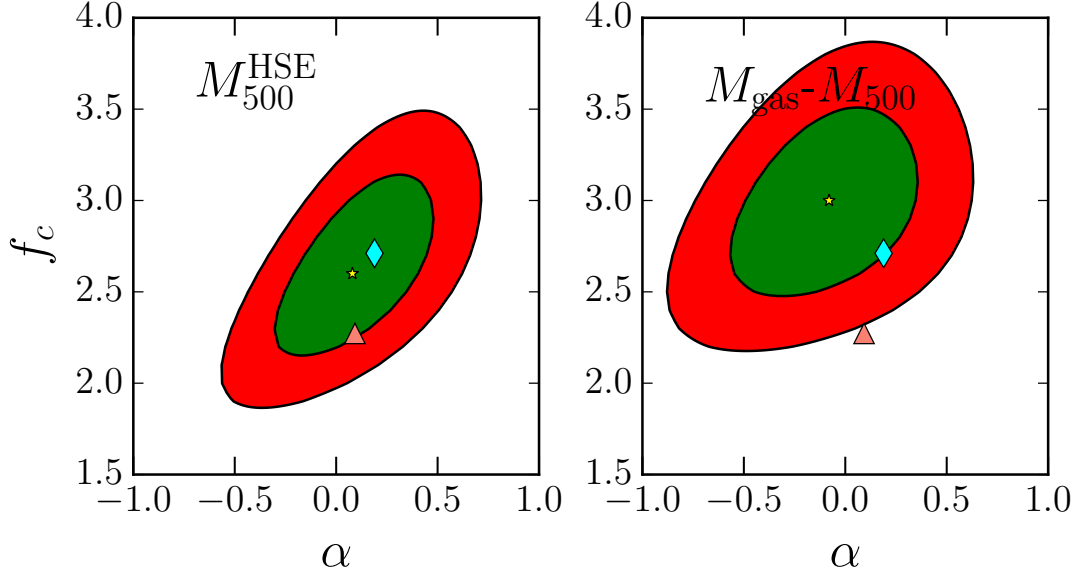
Figure 17. Effects of variations in the halo mass and concentration relation on the NFW scaling results, for the HSE and gas mass cases, respectively. Here we parametrized the variations as $c(M) \propto M^\alpha$ (Eq. 25), and then minimized the d^2-value with varying the normalization and mass slope parameters. The star symbol denotes the best-fit model. The two contours correspond to the regions satisfying the conditions $\Delta d^2 = d^2_{\text{w-scaling}}(A, \beta) - d^2_{\text{w-scaling}}(A^{\text{best-fit}}, \beta^{\text{best-fit}}) = 2.3$ or 6.17, respectively. The diamond symbol in each panel shows the parameters for our fiducial model DK15 at the mean redshift of clusters, $z = 0.23$, while the triangle symbol denotes the parameters of Duffy et al. (2008).

50 clusters. We tested the prediction of Diemer & Kravtsov (2014) by using the fitting formula for a typical accretion history that is kindly made available to us by Surhud More (More et al. 2015). However, we found that the current datasets cannot discriminate the steepened profile and the NFW profile at the outer radii. This would be interesting to further explore with an enlarged sample of clusters.

3.7. *A residual bias in source redshift*

As we discussed above, our results imply that the X-ray inferred mass may systematically underestimate the true mass: we found a possible bias of 5% level, although it is not significant (at a 1σ level). Eq. (7) suggests that a 10% bias in halo mass corresponds to about 3% bias in the lensing amplitudes. This is a tiny amount, and may imply a residual error in the source redshift estimation. Due to the limited color information of the current data (mostly only 2 colors), we cannot resolve this, but a further study is definitely worth exploring. For the same reason, it is worth further looking into a possible remaining systematic error in the shape measurement.

4. CONCLUSION AND DISCUSSION

In this paper, we have developed a novel method of measuring the cluster lensing distortion profiles along the NFW prediction, one of the most important predictions of CDM structure formation model. The method measures the cluster lensing profiles by stacking the "scaled" amplitudes of background galaxy ellipticities as a function of the "scaled" centric radius according to the NFW prediction of each cluster. To apply this method to real data, we combined the independent datasets for a nearly mass-selected sample of 50 massive clusters that are the Subaru weak lensing catalog in Okabe et al. (2013) and their X-ray observables of *XMM* and/or *Chandra* satellites in Martino et al. (2014). Here we used the X-ray observables to infer the NFW parameters of each cluster; more precisely, we used the halo mass of each cluster based on the

halo mass proxy relation of X-ray observables, either the hydrostatic static equilibrium or the self-similar scaling relation of gas mass, and inferred the halo concentration from the *c-M* relation found in N-body simulations of DK15. We found a 4 – 6σ level evidence of the existence of universal NFW profile in the 50 massive clusters (see Eq. 23 and Figures 8 – 11). To derive these results we have carefully studied a proper radial binning of the lensing distortion measurement and how to define the representative central value of each radial bin taking into account the cluster-centric distances and the lensing weights of background galaxies in the annulus. Our results give a proof of concept of the method we developed in this paper.

However, the improvement in the scatters of 50 cluster distortion profiles due to the NFW scaling analysis is not as much as expected from theory using simulations of cluster based on high-resolution *N*-body simulations (Figures 14 and 15). We discussed that, in order to reconcile the difference between the measurements and the simulation expectation, we need to introduce additional halo mass scatters to each cluster, by an amount of $\sigma(M)/M \sim 0.2$–0.3 (see Figure 15). This implies intrinsic scatters in the halo mass and X-ray observable relation (Okabe et al. 2010b). We also argued that the discrepancy might be due to an imperfect halo mass proxy relation of the X-ray observables (see § 3.4). Hence it would be worth further exploring the method by combining different observables of clusters. A promising example is the Sunyaev-Zel'dovich (SZ) effect. By using or combining the X-ray, optical richness and SZ effects to develop a well-calibrated relation between halo mass and cluster observables for a suitable sample of massive clusters, we can explore a further improvement in constraining the universality of cluster mass distribution. In addition, we throughout used the model *c-M* relation to infer the halo concentration of each cluster. In other words, we ignored intrinsic scatters of halo concentration that is known to exist even for halos of a fixed mass scale from simulation

based studies. If we can use observables to estimate halo concentration for each cluster, it might improve the NFW scaling results. For example, the concentration of member galaxies might be a good proxy of halo concentration on individual cluster basis. This would be worth exploring.

Our method offers various applications. First, we inversely use the weak lensing analysis of NFW scaling to infer the underlying true relation between halo mass and cluster observables. We made the initial attempt of this possibility in § 3.4. Since the NFW scaling method up- or down-weights less or more massive clusters in order to make their profiles to be in the similar amplitudes, it can be applied to halos over a wider range of mass scales as long as the clusters in the sample follow the universal NFW profile. In this sense this method would be less sensitive to the selection effect of clusters in a sample. Secondly, we can use this method to explore the underlying true form of the halo mass profile or the halo mass scaling relation with observables, as we attempted in § 3.5. As claimed in Diemer & Kravtsov (2014), massive clusters might display a steeper profile at the outer radii around or beyond the virial radius than predicted by NFW model, depending on the mass accretion history. By subdividing clusters into subsamples using a proxy to infer the mass accretion history, e.g. high or low concentration, we can use the NFW scaling analysis to explore the deviations from NFW prediction at the outer radii. This is a direct test of the hierarchical CDM structure formation model, and will be very interesting to explore.

The weak lensing measurements of 50 massive clusters we used in this paper seem to be still limited by statistics, mainly due to a low number density of background galaxies, which we needed to take in order to define a secure sample of background galaxies based on two passband data alone. Hence our method can be further improved by increasing background galaxies, based on photo-z information of more color information (Medezinski et al. 2013). We can also combine the lensing magnification bias measurement to improve the statistics. On-going wide-area optical surveys such as the HSC survey and the DES survey promise to provide us with a much larger, well-calibrated sample of massive clusters, so it would be interesting to apply the method developed in this paper to those datasets in combination with other wavelength surveys such as X-ray or SZ effects.

ACKNOWLEDGMENTS

REFERENCES

Adhikari, S., Dalal, N., & Chamberlain, R. T. 2014, JCAP, 11, 19
Bartelmann, M. 1996, A&A, 313, 697
Becker, M. R., & Kravtsov, A. V. 2011, ApJ, 740, 25
Bhattacharya, S., Habib, S., Heitmann, K., & Vikhlinin, A. 2013, ApJ, 766, 32
Böhringer, H., et al. 2004, A&A, 425, 367
Broadhurst, T., Takada, M., Umetsu, K., Kong, X., Arimoto, N., Chiba, M., & Futamase, T. 2005, ApJ, 619, L143
Bullock, J. S., Kolatt, T. S., Sigad, Y., Somerville, R. S., Kravtsov, A. V., Klypin, A. A., Primack, J. R., & Dekel, A. 2001, MNRAS, 321, 559
Clowe, D., Bradač, M., Gonzalez, A. H., Markevitch, M., Randall, S. W., Jones, C., & Zaritsky, D. 2006, ApJ, 648, L109
Dalal, N., Lithwick, Y., & Kuhlen, M. 2010, ArXiv e-prints:1010.2539
Davis, M., Efstathiou, G., Frenk, C. S., & White, S. D. M. 1985, ApJ, 292, 371
Diemer, B., & Kravtsov, A. V. 2014, ApJ, 789, 1
—. 2015, ApJ, 799, 108 (DK15)
Duffy, A. R., Schaye, J., Kay, S. T., & Dalla Vecchia, C. 2008, MNRAS, 390, L64
Ebeling, H., Edge, A. C., Allen, S. W., Crawford, C. S., Fabian, A. C., & Huchra, J. P. 2000, MNRAS, 318, 333
Ebeling, H., Edge, A. C., Bohringer, H., Allen, S. W., Crawford, C. S., Fabian, A. C., Voges, W., & Huchra, J. P. 1998, MNRAS, 301, 881
Einasto, J. 1965, Trudy Astrofizicheskogo Instituta Alma-Ata, 5, 87
Golse, G., & Kneib, J.-P. 2002, A&A, 390, 821
Hoekstra, H., Herbonnet, R., Muzzin, A., Babul, A., Mahdavi, A., Viola, M., & Cacciato, M. 2015, MNRAS, 449, 685
Hoekstra, H., Mahdavi, A., Babul, A., & Bildfell, C. 2012, MNRAS, 427, 1298
Hu, W., & Kravtsov, A. V. 2003, ApJ, 584, 702
Johnston, D. E., et al. 2007, ArXiv e-prints:0709.1159
Kaiser, N. 1986, MNRAS, 222, 323
Kneib, J.-P., et al. 2003, ApJ, 598, 804
Leauthaud, A., et al. 2010, ApJ, 709, 97
Mahdavi, A., Hoekstra, H., Babul, A., Bildfell, C., Jeltema, T., & Henry, J. P. 2013, ApJ, 767, 116
Mandelbaum, R., Slosar, A., Baldauf, T., Seljak, U., Hirata, C. M., Nakajima, R., Reyes, R., & Smith, R. E. 2013, MNRAS, 432, 1544
Mandelbaum, R., Tasitsiomi, A., Seljak, U., Kravtsov, A. V., & Wechsler, R. H. 2005, MNRAS, 362, 1451
Martino, R., Mazzotta, P., Bourdin, H., Smith, G. P., Bartalucci, I., Marrone, D. P., Finoguenov, A., & Okabe, N. 2014, MNRAS, 443, 2342
Masaki, S., Hikage, C., Takada, M., Spergel, D. N., & Sugiyama, N. 2013, MNRAS, 433, 3506
Medezinski, E., et al. 2013, ApJ, 777, 43
Meneghetti, M., Rasia, E., Merten, J., Bellagamba, F., Ettori, S., Mazzotta, P., Dolag, K., & Marri, S. 2010, A&A, 514, A93
Meneghetti, M., et al. 2014, ArXiv e-prints:1404.1384
Merritt, D., Graham, A. W., Moore, B., Diemand, J., & Terzić, B. 2006, AJ, 132, 2685
Merten, J., et al. 2014, ArXiv e-prints:1404.1376
Miyatake, H., et al. 2013, ArXiv e-prints:1311.1480
Miyazaki, S., et al. 2002, PASJ, 54, 833
More, S., Diemer, B., & Kravtsov, A. 2015, ArXiv e-prints
Navarro, J. F., Frenk, C. S., & White, S. D. M. 1996, ApJ, 462, 563
—. 1997, ApJ, 490, 493
Navarro, J. F., et al. 2004, MNRAS, 349, 1039
Newman, A. B., Treu, T., Ellis, R. S., Sand, D. J., Nipoti, C., Richard, J., & Jullo, E. 2013, ApJ, 765, 24
Oguri, M., Bayliss, M. B., Dahle, H., Sharon, K., Gladders, M. D., Natarajan, P., Hennawi, J. F., & Koester, B. P. 2012, MNRAS, 420, 3213
Oguri, M., & Takada, M. 2011, Phys. Rev. D, 83, 023008
Oguri, M., Takada, M., Umetsu, K., & Broadhurst, T. 2005, ApJ, 632, 841
Okabe, N., Smith, G. P., Umetsu, K., Takada, M., & Futamase, T. 2013, ApJ, 769, L35
Okabe, N., Takada, M., Umetsu, K., Futamase, T., & Smith, G. P. 2010a, PASJ, 62, 811
Okabe, N., Zhang, Y.-Y., Finoguenov, A., Takada, M., Smith, G. P., Umetsu, K., & Futamase, T. 2010b, ApJ, 721, 875

Okabe, N., et al. 2014, PASJ, 66, 99

Planck Collaboration et al. 2015, ArXiv e-prints

Power, C., Navarro, J. F., Jenkins, A., Frenk, C. S., White, S. D. M., Springel, V., Stadel, J., & Quinn, T. 2003, MNRAS, 338, 14

Rozo, E., et al. 2009, ApJ, 699, 768

—. 2010, ApJ, 708, 645

Schneider, P. 2006, in Saas-Fee Advanced Course 33: Gravitational Lensing: Strong, Weak and Micro, ed. G. Meylan, P. Jetzer, P. North, P. Schneider, C. S. Kochanek, & J. Wambsganss, 1–89

Smith, G. P., Kneib, J.-P., Smail, I., Mazzotta, P., Ebeling, H., & Czoske, O. 2005, MNRAS, 359, 417

Springel, V. 2005, MNRAS, 364, 1105

Springel, V., Yoshida, N., & White, S. D. M. 2001, New Astron., 6, 79

Stanek, R., Rasia, E., Evrard, A. E., Pearce, F., & Gazzola, L. 2010, ApJ, 715, 1508

Takada, M., & Spergel, D. N. 2014, MNRAS, 441, 2456

Takahashi, R., Sato, M., Nishimichi, T., Taruya, A., & Oguri, M. 2012, ApJ, 761, 152

Tyson, J. A., & Fischer, P. 1995, ApJ, 446, L55

Umetsu, K., et al. 2014, ArXiv e-prints:1404.1375

van den Bosch, F. C., More, S., Cacciato, M., Mo, H., & Yang, X. 2013, MNRAS, 430, 725

Vikhlinin, A., et al. 2009, ApJ, 692, 1060

von der Linden, A., et al. 2014, MNRAS, 439, 2

Wechsler, R. H., Bullock, J. S., Primack, J. R., Kravtsov, A. V., & Dekel, A. 2002, ApJ, 568, 52

Wittman, D., Dawson, W., & Benson, B. 2014, MNRAS, 437, 3578

Zhang, Y.-Y., Finoguenov, A., Böhringer, H., Kneib, J.-P., Smith, G. P., Kneissl, R., Okabe, N., & Dahle, H. 2011, A&A, 527, C3

Zhang, Y.-Y., et al. 2010, ApJ, 711, 1033

Zhao, D. H., Jing, Y. P., Mo, H. J., & Börner, G. 2009, ApJ, 707, 354

Zhao, D. H., Mo, H. J., Jing, Y. P., & Börner, G. 2003, MNRAS, 339, 12

Zitrin, A., et al. 2014, ArXiv e-prints:1411.1414